

Offshore and Onshore Power curve characterization for ground-generation AWES

Markus Sommerfeld¹, Martin Dörenkämper², Jochem De Schutter³, and Curran Crawford¹

¹Institute for Integrated Energy Systems, University of Victoria, British Columbia, Canada

²Fraunhofer Institute for Wind Energy Systems, Oldenburg, Germany

³Systems Control and Optimization Laboratory IMTEK, Freiburg, Germany

Correspondence: Markus Sommerfeld (msommerf@uvic.ca)

Abstract.

Airborne wind energy systems (AWESs) ~~aim to~~ are nominally envisaged to operate at altitudes well above conventional wind turbines (WTs) and harvest energy from stronger winds aloft. While multiple AWES concepts compete for entry into the market, this study focuses on ground-generation AWES. Various companies and researchers proposed power curve characterizations for AWES, but no consensus for an industry-wide standard has been reached. A universal description of a ground-generation AWES power curve is difficult to define, because of complex tether ~~and drag losses as well as~~ and misalignment losses subject to alternating flight paths and wind conditions which lead to significant changes in the average cycle power (which is different from the optimal power predicted by simple models). ~~over changing wind conditions with altitude, as~~ compared to conventional WT with winds at fixed hub height] and rotor area normalization. ~~Therefore,~~ this study determines AWES power and annual energy production (AEP) based on the `awebox` optimal control model for two AWES sizes, driven by representative 10-minute onshore and offshore mesoscale WRF wind data. The wind resource is analyzed with respect to atmospheric stability as well as annual and diurnal variation. The wind data is categorized using k-means clustering, to reduce the computational cost. The impact of changing wind conditions on AWES trajectory and power cycle is investigated. Optimal operating heights are below 400 m onshore and below 200 m offshore. ~~Efforts are made to derive AWES power coefficients similar to conventional WT to enable a simple power and AEP estimation for a given site and system. This AWES power coefficient decreases up to rated power due to the increasing tether length with wind speed and the accompanying tether losses. A comparison between different AEP estimation methods shows that a low number of clusters with three representative wind profiles within the clusters yields the highest AEP, as other wind models average out high wind speeds which are responsible for a high percentage of the overall AEP.~~ We compare AWES power curve descriptions and estimate AEP based on wind speed probability distributions over various reference heights. These results are compared to quasi steady-state (QSS) AWES and WT reference models. The optimized power curves show a delay in rated wind speed which can be attributed to increased tether losses which are not captured by simplified model. Offshore AEP is generally higher than onshore, but lower wind shear weakens the argument for higher operating altitudes for AWES compared to conventional WT.

1 Introduction

25 General, Mark: too little attention on 'what is new' i.e. AEP calculation. Should be described in more detail & add 'strong foundation'. No proof that AEP is realistic. Remove c_p calculation
paper reads like a draft version. More precise writing and better choice of words. more conservative formulation (page 10 line 192: cluster mean profiles that show decreasing wind speed above a certain height could be the result from choosing too many clusters. As these type of profiles are not covered by log/power law profiles, I would think that the
30 added value of the clustering approach (and thus your methodology) is that you can identify such profiles from the data.
)
line 372 (page 20) you briefly discuss the offshore WT tower design. This is a bit distracting and not adding a lot of value.

Mark: restructure Introduction e.g. objective / contribution not clear, not very informative about related literature
35 on AWE yield assessment, role of clustering not clear Airborne wind energy systems (AWESs) aspire to harvest stronger and less turbulent winds at mid-altitude, here defined as heights above 100 m and below 1500 m, ~~which are unreachable~~ and beyond what is achievable with conventional wind turbines (WTs). The prospects of higher energy yield combined with reduced capital cost motivate the development of this novel class of renewable energy technology Lunney et al. (2017); Fagiano and Milanese (2012). Unlike conventional ~~wind turbines~~ WTs, which have converged to a single concept with three blades ~~, nacelle and~~
40 ~~generator supported by~~ and a conical tower, several different AWES designs are under investigation by numerous companies and research institutes Cherubini et al. (2015). These kite-inspired systems consist of three main components: a flying wing or kite, a ground station and a tether to connect them. Various concepts compete for entry into the market. This study focuses on the two-phase, ground-generation concept, also referred to as pumping-mode which is the main ~~route~~ concept that industry is investigating. During the reel-out phase the wing pulls a non-conductive tether from a drum on the ground which is connected
45 to a generator, thereby producing electricity. ~~During the reel-in phase the wing reduces its aerodynamic forces by adjusting the angle of attack to reduce the power needed to pull the tether back in.~~ This is then followed by the reel-in phase during which the wing adjusts its angle of attack to reduce aerodynamic forces and returns to its initial position. Other concepts such as fly-gen, aerostat or rotary lift are not within the scope of this study Cherubini et al. (2015).

Since this technology is still in an early stage, validation and comparison of results is difficult. A standardized power curve
50 definition would enable comparison between different AWES concepts and to conventional wind turbines. Together with the site-specific wind resource, power curves help wind park planners and AWES device manufacturers to estimate ~~the~~ annual energy production (AEP) and determine financial viability Malz et al. (2020). As such this work supports the development and implementation of this novel technology .

In contrast to a conventional WT, the power output of an AWES is highly dependent on the complete wind speed ~~magnitude~~
55 ~~and~~ profile shape (wind speed and direction variation with height) ~~which determines the power output as well as~~ as system performance is governed by optimal operating ~~altitude and~~ trajectories over the wind profile altitude range rather than primarily by a hub-height windspeed. Simple wind profile approximations using logarithmic or exponential wind speed profiles, which

are often erroneously applied beyond earth's surface layer Optis et al. (2016), might approximate long-term average conditions, but can not capture the broad variation of profile shapes [that exist on short timescales](#) Emeis (2018). They are therefore an inappropriate approximation to estimate instantaneous, diurnal and seasonal variation in electrical power output. However, they are the standard in most AWES power estimation studies (e.g. Leuthold et al. (2018); Licitra et al. (2019); De Schutter et al. (2018); Aull et al. (2020)). [An alternative approach to estimating AWES energy production using the ERA5 global reanalysis wind data set can be found in](#) Schelbergen et al. (2020a).

AWES need to dynamically adapt their flight trajectory to changing winds in order to optimize power production. Wind ~~conditions are determined~~ [velocity profiles are governed](#) by environmental, location-dependent conditions (e.g. surface roughness) and weather phenomena on a multitude of temporal and spatial scales, subject to diurnal and seasonal patterns. [The preferable means of determining wind conditions are long-term, high resolution measurements, which at mid-altitudes can solely be achieved by long-range LiDAR.](#) ~~They can be estimated from~~ Numerical mesoscale weather prediction models such as the weather research and forecasting model (WRF), which is well known for conventional WT siting applications Salvação and Guedes Soares (2018); Dörenkämper et al. (2020), [are used to estimate wind conditions on time scales of a few minutes to years.](#) These numerical simulations should be corrected for systematic errors using measurements from ~~light detection and ranging~~ LiDAR during site assessment and deployment. ~~Results~~ [Data](#) in this study are exclusively based on WRF mesoscale simulations, since measuring wind conditions at mid-altitudes is difficult due to reduced data availability Sommerfeld et al. (2019a) and measurements are hard to find, [typically being](#) proprietary ~~or confidential~~. We compare [conventional WT hub-height based power curves to optimal](#) AWES performance for an onshore location in northern Germany near the city of Pritzwalk Sommerfeld et al. (2019b) and an offshore location at the FINO3 research platform in the North Sea. [A key contribution of this paper is to account for the detailed variation in wind profiles and associated optimal flight trajectories in generating a power curve characteristic for AWES. To achieve this goal, we cluster the simulated wind velocity vectors using a k-means clustering algorithm. Through clustering, we avoid the excessive computational cost of computing optimal trajectories for each](#) [10 min average profile, but maintaining a representative data set that encapsulates the important wind profile characteristics.](#) [The clustered profiles are also used to generate AEP estimates. Standard logarithmic wind profiles are compared as reference calculations.](#)

[Optimal AWES trajectories are generated using the awebox optimization framework, assuming simplified mass scaling. In summary, this manuscript provides insight into typical onshore and offshore wind conditions up to 1000 m, their variation and the potential application of clustering to identify representative wind speed profiles and in turn yield more realistic power and energy estimation. Our results show that optimal operating heights are generally between 150 and 500 m and](#) [Add conclusion to AEP & power curve after analysis of new kappa=2.4 data](#)

~~Section 2 describes the onshore and offshore wind resource based on the WRF model. Sub-sections give a brief overview of the WRF model and compare wind statistics.~~ [Section 2 introduces the WRF model set-up and generated compares the onshore and offshore wind resource.](#) Section 3 introduces the k-means clustering algorithm and summarizes results of clustered wind velocity profiles (both longitudinal and lateral wind components). These include cluster averaged profiles and correlation with seasonal, diurnal and atmospheric stability. Section 4.3 introduces the awebox optimization framework. It summarizes

aircraft, tether and ground station models as well as system constraints and initialization used to ~~derive~~ produce the results shown in section 5. ~~This includes~~ These include flight paths and time series of various performance parameters, and a statistical analysis of tether length and operating altitude. Furthermore, we compare power curve characterization, capacity factor and AEP estimates. Based on these results, an AWES power coefficient is defined to approximate AWES efficiency and power based on system size and wind speed. Finally, Section 6 concludes with an outlook and motivation for future work.

2 Wind data

This study compares the general AWES performance and power curves at ~~two a~~ representative onshore and offshore locations in Europe (see fig 1). Wind conditions for the chosen years are assumed to be representative of that location. “Onshore” wind data at the Pritzwalk Sommersberg airport (lat: 53°10′47.00″N, lon: 12°11′20.98″E) in northern Germany and comprises 12 months of WRF simulation between September 2015 and September 2016. The area surrounding the airport mostly consists of flat agricultural land with the town of Pritzwalk to the south and is therefore a fitting location for wind energy generation (See Sommerfeld et al. (2019a) and Sommerfeld et al. (2019b) for details). The FINO3 research platform in the North Sea (lat: 55°11,7′N, lon: 7°9,5′ E) was chosen as a representative “offshore” location due to the proximity to several offshore wind farms and the amount of comprehensive reference measurements Peña et al. (2015). The offshore simulation covers the time frame between September 2013 and September 2014.

2.1 Mesoscale model

The mesoscale simulations in this study were carried out using the weather research and forecasting (WRF) model from Skamarock et al. (2008). The onshore simulation was performed with version 3.6.1 before the 2018 release of WRF version 4.0.2¹ in which the offshore simulations were computed. The setup of the model has been adapted and constantly optimized for wind energy applications by the authors ~~in~~ with the framework of various projects and applications in recent years Dörenkämper et al. (2015, 2017); Dörenkämper et al. (2020); Hahmann et al. (2020); Sommerfeld et al. (2019b).

The focus of this study is not on the detailed comparison between mesoscale models, but on AWES performance subject to representative onshore and offshore wind conditions determined based on clustered wind profiles (described ~~on~~ in section 3). ~~To that end~~ Both WRF models provide adequate wind data for ~~our purposes~~ for the assessment of AWES performance, even though the setup and time frame are different. ~~data~~ Both simulations consist of three nested domains centered around either the FINO3 met mast (see Figure 1) or the Pritzwalk Sommersberg airport. Atmospheric boundary conditions are defined by ERA-Interim Dee et al. (2011) for the onshore location and by ERA5 Hersbach and Dick (2016) reanalysis data for the offshore location, while sea surface parameters for the offshore location are based on OSTIA Donlon et al. (2012). These data sets have proven to provide good results for wind energy relevant heights and sites Olauson (2018); Hahmann et al. (2020). Both simulations use the MYNN 2.5 level scheme for the planetary boundary layer (PBL) physics Nakanishi and Niino (2009). While the onshore simulation was performed in one 12 month simulations (01.09.2015 - 31.08.2016), the offshore simulation

¹WRF model releases: <https://github.com/wrf-model/WRF/releases>

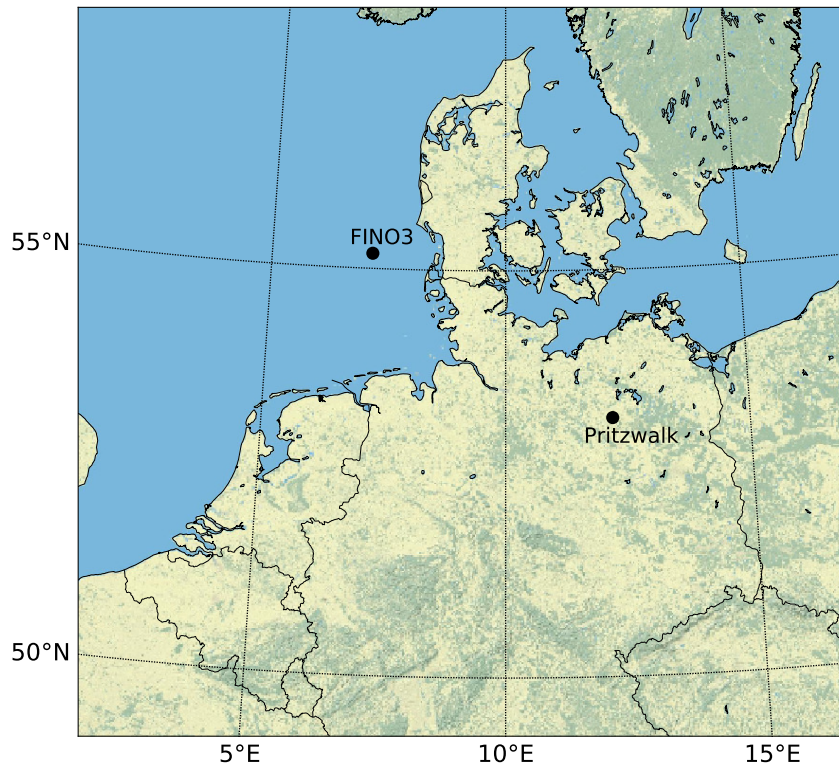


Figure 1. Topography Map of northern Germany with the representative onshore (Pritzwalk) and offshore (FINO3) locations highlighted by black dots.

125 period consisted of 410 days (30.08.2013 - 14.10.2014) that were split into 41 simulations of 10 days each with an additional 24 hours of spin-up time per run. The data from the mesoscale models' sigma levels (terrain-following) were transformed to the geometric heights using the post-processing methodology described in Dörenkämper et al. (2020). Table 1 summarizes the key parameters of the model settings used in this study. All simulations were run on the *EDDY*² High-Performance Computing clusters at the University of Oldenburg.

²EDDY: HPC cluster at the Carl von Ossietzky Universität Oldenburg, see: <https://www.uni-oldenburg.de/fk5/wr/hochleistungsrechnen/hpc-facilities/eddy/>

Table 1. Key setup parameters of the onshore and offshore mesoscale model simulations

Model Parameter	Settings	
	Onshore	Offshore
WRF model version	3.5.1	4.0.2
time period	01.09.2015 - 31.08.2016	30.08.2013 - 14.10.2014
Reanalysis	ERA-Interim	ERA5 & OSTIA
Horizontal grid size (D01, D02, D03)	120x120, 121x121, 121x121	150x150, 151x151 , 151x151
Resolution (D01, D02, D03)	27 km, 9 km, 3 km	18 km, 6 km, 2 km
Vertical levels	60 sigma levels (about 25 below 2 km)	60 sigma levels (about 25 below 2 km)
Nesting	1-way	1-way
Initialisation strategy	single run	240 h runs plus 24 h spinup time
Nudging	Analysis nudging (FDDA)	Analysis nudging (FDDA)
PBL scheme	MYNN level 2.5 scheme	MYNN level 2.5 scheme
Micro physics	Ferrier scheme	WRF Single–moment 5–class scheme
Long wave & shortwave radiation	RRTM & Dudhia	RRTMG scheme

2.2 Wind regime

130 Figure 2 depicts the wind roses of the annual wind conditions at 100 (top) and 500 m (bottom) height onshore (left) and offshore (right). The dominant wind direction at both locations is **S** southwest, ~~rotating from Southwest to West~~ turning clockwise with increasing altitude.

Directional variability decreases and wind speed increases with height, following the expected trends in the northern hemisphere Arya and Holton (2001); Stull (1988). The average onshore wind direction ~~rotates~~ turns about 14° between 100 and
135 500 m, whereas average offshore wind direction only ~~changes~~ veers approximately 5°. The offshore wind direction conditions ~~veer~~ turns approximately about 10° additional degrees above 500 m, resulting in roughly the same westerly wind direction at high altitudes at around 1000 m. Due to prevailing unstable conditions offshore, a strong mixing with height is found resulting in less veer across the heights investigated in this study. ~~The relative wind speed increase of~~ The wind shear at the offshore location is lower compared to the onshore location due to lower surface roughness ~~and the already high wind speeds at lower~~
140 heights.

Figure 3 shows the annual horizontal wind speed probability ~~distribution~~ distributions at each individual height level for both locations. ~~These statistics give an insight into the overall wind conditions, but the actual profile shapes;~~ These distributions give an insight into the wind speed statistics at individual heights, but not into the statistics of the wind profile shapes, which are important for AWES power and trajectory optimization. ~~are lost in this evaluation.~~ The chosen nonlinear color range allows
145 for the representation of the entire relative probability range. Onshore (left) wind speeds are relatively low and have a fairly

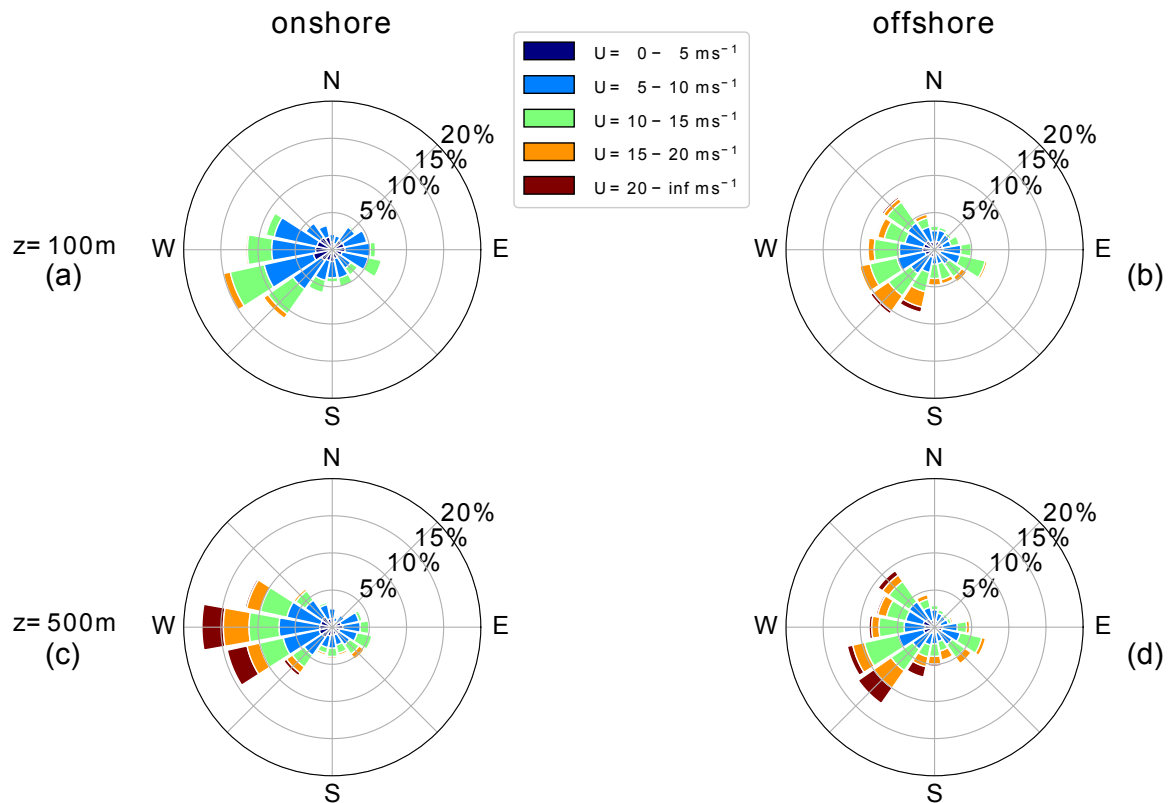


Figure 2. Annual ~~onshore and offshore~~ wind direction and speed statistics ~~for 100 and 500 m~~ at [Pritzwalk \(onshore\)](#) and [FINO3 \(offshore\)](#) presented as wind roses [for 100 and 500 m](#). ~~On average wind direction onshore rotates about 14° while offshore winds rotate about 5° between 100 and 500 m.~~ ~~Onshore shows a higher wind shear due to higher surface roughness and relatively high wind speeds offshore.~~ Markus: added abcd

narrow range below 300 m, due to dominant surface effects. Above this height the distribution broadens, but a high probability of low wind speeds remains ~~up to high altitudes~~ [for the full height range](#). ~~This leads to the development of~~ [The distributions show](#) bimodal characteristics caused by different atmospheric stratification. Low wind speeds are commonly associated with unstable and high wind speeds with neutral or stable atmospheric conditions (see sub-section 3.2).

150 Such multimodal distributions at higher altitudes are better described by the sum of two or more probability distributions, as standard Weibull or Rayleigh distributions can not capture this phenomenon Sommerfeld et al. (2019a). Offshore (right) wind speeds on the other hand have a wider distribution at all heights as they are less inhibited by surface effects. Similar to onshore, the offshore frequency distribution also shows a high probability of lower wind speeds (between 5-10 ms^{-1}) at all heights. ~~As mentioned above, the relative wind speed increase with height is less pronounced offshore than onshore.~~ Higher wind speeds at lower altitudes benefits conventional WT and weakens the argument for offshore AWES as one of their benefits
 155 wind speeds at lower altitudes benefits conventional WT and weakens the argument for offshore AWES as one of their benefits would be to harness energy from the stronger winds at higher altitudes. ~~However, offshore AWES will also benefit from higher~~

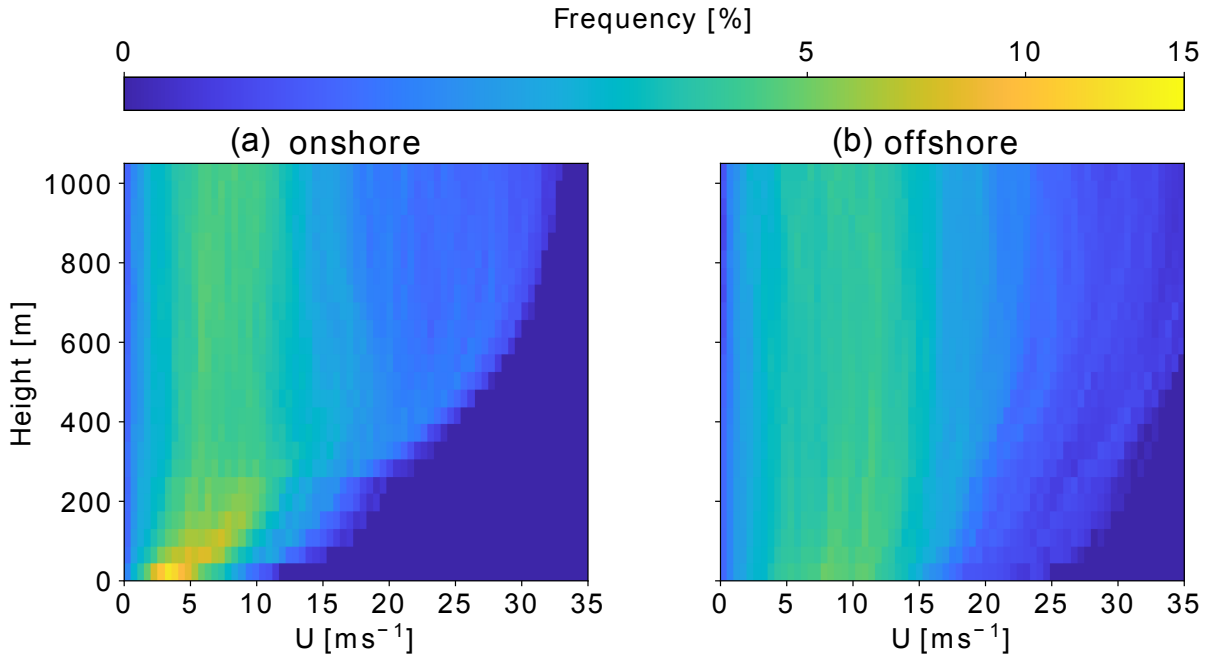


Figure 3. Comparison of WRF-simulated annual wind speed probability distribution at each height level between Pritzwalk (onshore left) and FINO3 (offshore right) up to 1000 m. A nonlinear color scheme was chosen to represent the high probability of low altitude onshore winds while still differentiating the lower, wide spread frequencies at higher altitudes. **Markus: added a,b;**

~~offshore winds and move offshore for other reasons such as safety or land use regulations.~~ Nevertheless, also AWES benefit from these higher wind speeds. Additional reasons for placing AWES offshore are safety and land use regulations and potential cost benefits of smaller support structure. If AWES can reliably operate autonomously they might still provide a cheaper source of electricity than conventional WT, due to their reduced material cost. ~~Another benefit of offshore AWES in comparison to conventional WT is the smaller and cheaper support structure.~~ Atmospheric stability of the boundary layer, which highly affects the wind speed profile shape, is commonly ~~eategorized~~ characterized using the Obukhov length \mathcal{L} Obukhov (1971); Sempreviva and Gryning (1996). Here the application is extended to mid-altitudes. \mathcal{L} is defined by the simulated friction velocity u_* , virtual potential temperature θ_v , potential temperature θ , kinematic virtual sensible surface heat flux Q_S , kinematic virtual latent heat flux Q_L , the von Kármán constant k and gravitational acceleration g :

$$\mathcal{L} = \left(\frac{-u_*^3 \theta_v}{kg} \right) \left(\frac{1}{Q_S} + \frac{0.61}{Q_L \theta} \right). \quad (1)$$

Various stability classifications using Obukhov length are defined for different wind energy sites. Table 2 summarizes the Obukhov length bin widths Floors et al. (2011) and the frequency of occurrence of each stability class onshore and offshore, consistent with Sommerfeld et al. (2019b) ~~We chose The same classification as in~~ Sommerfeld et al. (2019b) ~~for consistency.~~ Neutral stratification occurs approximately 20% of the year at both locations. The lower heat capacity of the land surface leads

to a faster heat transfer and a quicker surface cool-off which favors the development of stable stratification ($\approx 17\%$ onshore vs $\approx 6\%$ offshore). The offshore location has a higher probability of unstable conditions which is likely caused by a warmer ocean surface compared to the air above Archer et al. (2016).

Table 2. Stability classes based on Obukhov lengths Floors et al. (2011) and associated annual ~~onshore and offshore~~ probability [at Pritzwalk \(onshore; 01.09.2015 - 31.08.2016\)](#) and [FINO3 \(offshore; 30.08.2013 - 14.10.2014\)](#), based on WRF results.

Stability class	\mathcal{L} [m]	onshore	offshore
Unstable (U)	$-200 \leq \mathcal{L} \leq -100$	7.27%	13.66%
Nearly unstable (NU)	$-500 \leq \mathcal{L} \leq -200$	7.09%	16.34%
Neutral (N)	$ \mathcal{L} \geq 500$	20.71%	22.82%
Nearly stable (NS)	$200 \leq \mathcal{L} \leq 500$	12.56%	5.15%
Stable (S)	$50 \leq \mathcal{L} \leq 200$	17.24%	6.20%
Very stable (VS)	$10 \leq \mathcal{L} \leq 50$	10.04%	2.96%
Other	$-100 \leq \mathcal{L} \leq 10$	25.09%	32.87%

Both unstable and stable conditions can lead to non-logarithmic and non-monotonic wind speed profiles. Unstable conditions are often accompanied by almost uniform wind speed profiles due to increased mixing, whereas low level jets (LLJs) can develop during the nocturnal stable onshore boundary layer Banta (2008). Both locations have a high chance of unassigned “other” conditions which are mostly associated with low wind speeds (see figure: 12).

3 Clustering of wind conditions

Mark: better structuring [The power output of](#) wind energy [systems](#) in general and AWES in particular are ~~mainly affected~~ [by not only defined by the temporal and spatial averaged](#) wind velocity [and its evolution](#) , but are also [its variation in time and variation with height](#). Many temporal and spatial averages, correlations and approximations are used to describe the constantly varying wind conditions and their affect on the device. Instead [of reverting back to simple 1D approximations such as the logarithmic wind profile, here 10-minute, simulated,](#) representative wind velocity profiles are chosen ~~to avoid excessive averaging and to~~ compare AWES performance as realistically as possible. The onshore (Pritzwalk) and offshore (FINO3) data are classified to determine representative profiles. Classifying the wind regime using atmospheric stability is an accepted methodology to describe the near-surface atmosphere. A common [proxy metric](#) for atmospheric stability is the Obukhov length Obukhov (1971); Sempreviva and Gryning (1996), ~~a metric that~~ [which](#) exclusively uses surface data (see section 2.2 and equation 1). Previous studies Sommerfeld et al. (2019a, b) showed that Obukhov-length-classified wind speed profiles diverge with height, especially during neutral and stable conditions. This indicates vertically heterogeneous atmospheric stability and suggests that surface-based stability categorization is insufficient for higher altitudes. Clustering the wind speed or velocity profiles purely based on ~~data~~ [their](#) similarity on the other hand results in more cohesive profile groups (see figure A1 and A1 in the appendix) Schelbergen et al. (2020b). In contrast to classifying the wind regime by atmospheric stability, which requires

temperature and heat flux data, ~~mathematical~~ clustering only uses wind velocity or speed data at multiple heights and groups profiles by similarity. Therefore, clustering can also be applied to wind-only measurements such as LiDAR.

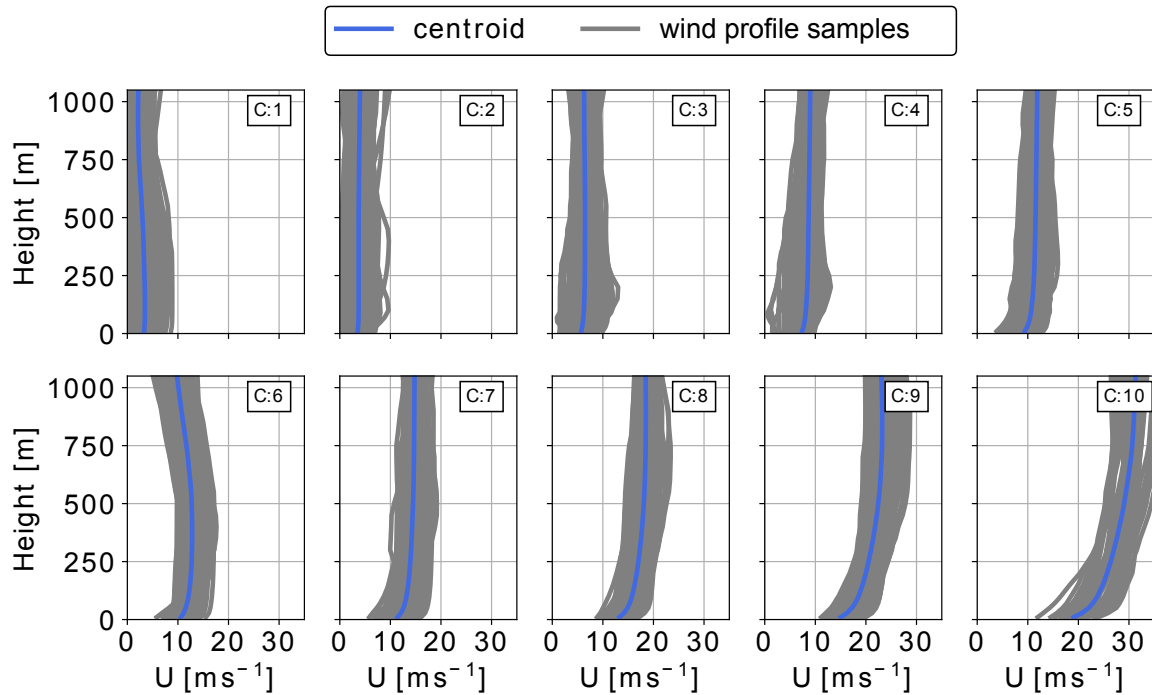


Figure 4. Clustered offshore wind velocity profiles (here shown as 2D projected wind speed profiles). The average profile or centroid is shown in blue while all the assigned profiles are shown in grey.

195 The k-means clustering algorithm Pedregosa et al. (2011) used in this study was chosen for its ease of use and scalability, due to the high dimensionality of the data set. Many other algorithms produce similar results, but a comparison between clustering algorithms is beyond the scope of this research.

Before clustering the two horizontal wind velocity components u and v , whose vertical variation define the wind velocity profile, are rotated such that the main wind component (average wind direction up to 500 m) u_{main} points in positive x direction and the deviation $u_{\text{deviation}}$ is perpendicular to it, pointing in positive y direction. This removes the directional dependency of the wind velocity profiles, allows for more homogeneous clusters and simplifies the comparison of `awebox` results. It is analogous to assuming omnidirectional operation while the flying wing still needs to adjust to wind condition which are changing with height. The algorithm assigns each data point, in our case wind velocity profile up to 1000 m, which compriseds of approximately 30 heights and 2 directions, to one of k clusters ~~defined~~ represented by their respective cluster mean also referred to as centroid. These centroids are ~~calculated~~ arranged such that they minimize the sum of the Euclidean distances (also referred to as “inertia” or “within-cluster sum-of-squares”), i.e. the cost function of the algorithm, ~~also-referred~~

205

to as “inertia” or “within-cluster sum-of-squares”, to every data point within each cluster. As such, the centroids are usually not actual data points, but rather the average of that cluster, and will at best coincide with a data point by chance. The resulting cluster labels are random results of initialization and are therefore insignificant. The cluster label number is random and does not have any mathematical meaning. Later evaluation uses clusters sorted by average wind speed up to 500 m. As presented, the resulting clusters are sorted by average wind speed up to 500 m.

Markus: re-write this section because clustering re-done! The variable k refers to the fixed, predefined number of clusters. The choice of k significantly affects the accuracy of the resulting power and AEP predictions (see section 5.4) as well as the computational cost associated with clustering (pre-processing) and AWES trajectory optimization (processing). The elbow method and silhouette score indicate preferable choices of k. The elbow method (see fig: 5 - top left) compares the inertia trends as a function of k. **Mark: Based on my own work, I don't expect an elbow/kink in the inertia line. Be more specific about why you choose the number of clusters**

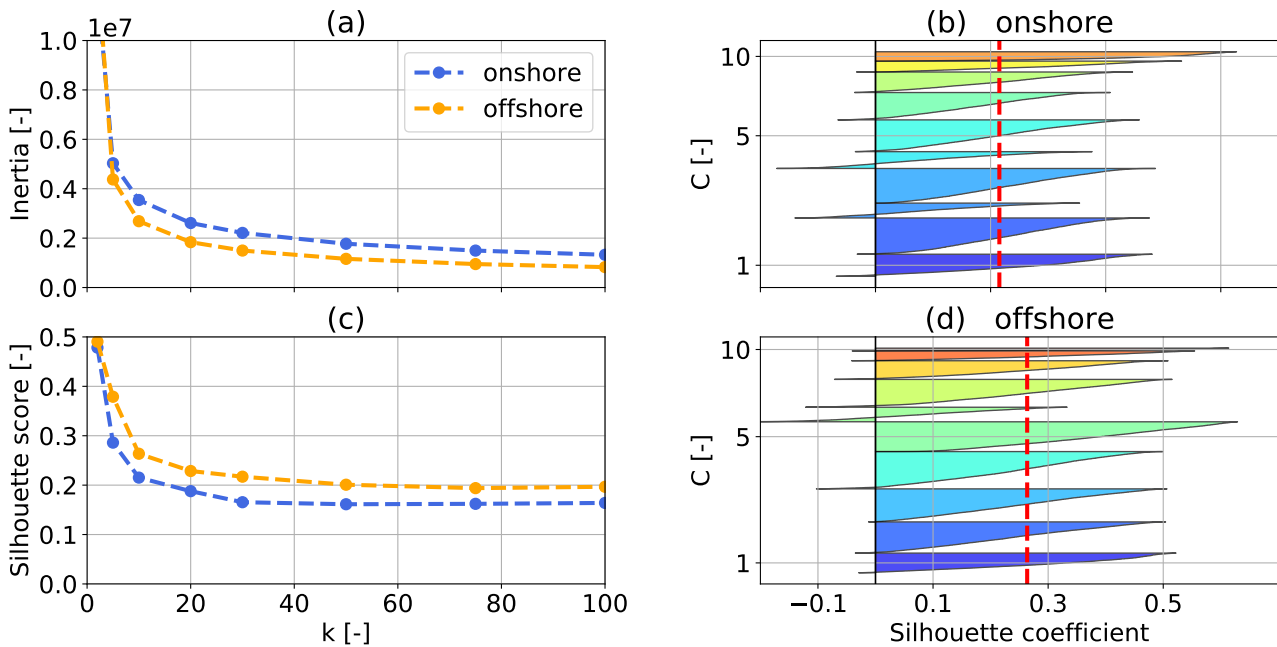


Figure 5. Top left: k-means clustering inertia over number of cluster k for one year of rotated onshore (blue) and offshore (orange) wind velocity profiles up to 1000 m. Bottom left: Silhouette score (average of the silhouette coefficients on the right) over number number of cluster k for both locations. Right: Silhouette coefficients (top onshore, bottom offshore) which express the distance to neighbouring clusters, for a representative k=10. Negative values indicate that the sample is closer to neighbouring clusters than to the one they are assigned to. The red dashed line represents the silhouette score. **Markus: remade & improved clustering results. Make sure figure still fits in text**

k is often chosen at a point where the inertia reduction becomes marginally small or decreases in a linear fashion with increasing number of clusters, often represented by a sharp bend or elbow in the inertia trend. Absolute values of inertia are

220 ~~somewhat meaningless as it is~~ not a normalized metric and therefore scales with size of the considered data set. ~~A majority of the difference between on- and offshore is likely due to different number of vertical grid cells which the algorithm interprets as dimensions (see table 4).~~ **Markus: now less difference because new classification scheme. Comment on the few clusters with more negative sil. coeff.** The silhouette coefficients on the other hand are normalized between -1 (worst) and 1 (best) and indicate the membership of a data point to its cluster in comparison to other clusters, i.e. proximity of each data point in one
225 cluster to data points in neighboring clusters. A negative value suggests that a data point is assigned to the wrong cluster. The silhouette score is the average of all silhouette coefficients for a fixed number of clusters k . Its trend is shown in the bottom left of figure 5 . The top right depicts the onshore and the bottom right the offshore silhouette coefficients for a representative k of 10. ~~Note that the clusters are unsorted as a result of the random initialization process.~~ Note that the order of the clusters is random and does not follow any logic. Therefore, their labels (1 to 10) are omitted on the y-axis of the right sub-figures in
230 figure 5. Silhouette coefficients and the resulting silhouette score illustrate that the offshore clusters are more coherent than the onshore clusters. ~~Onshore clusters also have more negative silhouette coefficients which could indicate too many or too few clusters~~ de Amorim and Hennig (2015); Kaufman and Rousseeuw (1990). ~~Another possible explanation could be that the continuous nature of wind which results in a high cluster proximity as well as the high variability of profile shapes onshore led to a worse score.~~ The following sub-section shows Figures A1 and 6 show that non-monotonic wind velocity profiles (e.g.
235 profiles with low level jets (LLJs)), which are more common onshore, intersect with other clusters and therefore reduce the overall silhouette score. We assume $k=20$ to be a reasonable choice for AWES power analysis, according to the elbow method and silhouette score. The impact of number of clusters on AEP is later discussed in sub-section 5.4. .

3.1 Analysis of clustered profiles

For visualization purposes, the following sub-sections describe the wind conditions at both locations using only $k=10$ clusters, instead of the $k=20$ clusters chosen to analyze AWES performance in section 5. Figure 6 (top) shows the average wind speed profiles of the clustered wind velocity profiles, also referred to as centroids. The ~~comprising wind speed profiles~~ magnitude of the WRF-simulated wind velocity profiles that define their respective cluster are depicted in grey. ~~The cluster assigned profiles span~~ Within a cluster, the wind speed profiles span a fairly narrow range of wind speeds except for a few outliers (see figure: A1, A1 in the appendix), indicating coherent clusters. Clusters are sorted by average centroid speed up to 500 m, represented
245 by their colors and labels ($C = 1 - 10$).

As expected offshore (right) low altitude wind speeds are higher and wind shear is lower than onshore (left). Overall, offshore centroids are wider spread ~~and distinct~~ in comparison to the onshore profiles ~~which explains the higher silhouette score (see figure 5).~~ The associated annual centroid frequency of occurrence for $k=10$ is shown below in figure 6. Wind speeds of the first and sixth offshore centroid decrease at higher altitude which could be caused by local or large-scale weather phenomenon. Both
250 these clusters have a comparatively low probability. ~~This could be caused by directional differences which are not depicted in a 2D wind speed plot, different large-scale weather phenomenon, or indicate the usage of too many clusters as both clusters have a very low probability.~~ The first three onshore and offshore clusters exhibit very low wind shear with almost constant wind speed above 200 m. Onshore cluster 5, which seems to comprise of non-monotonic profiles as its centroid has a distinct LLJ

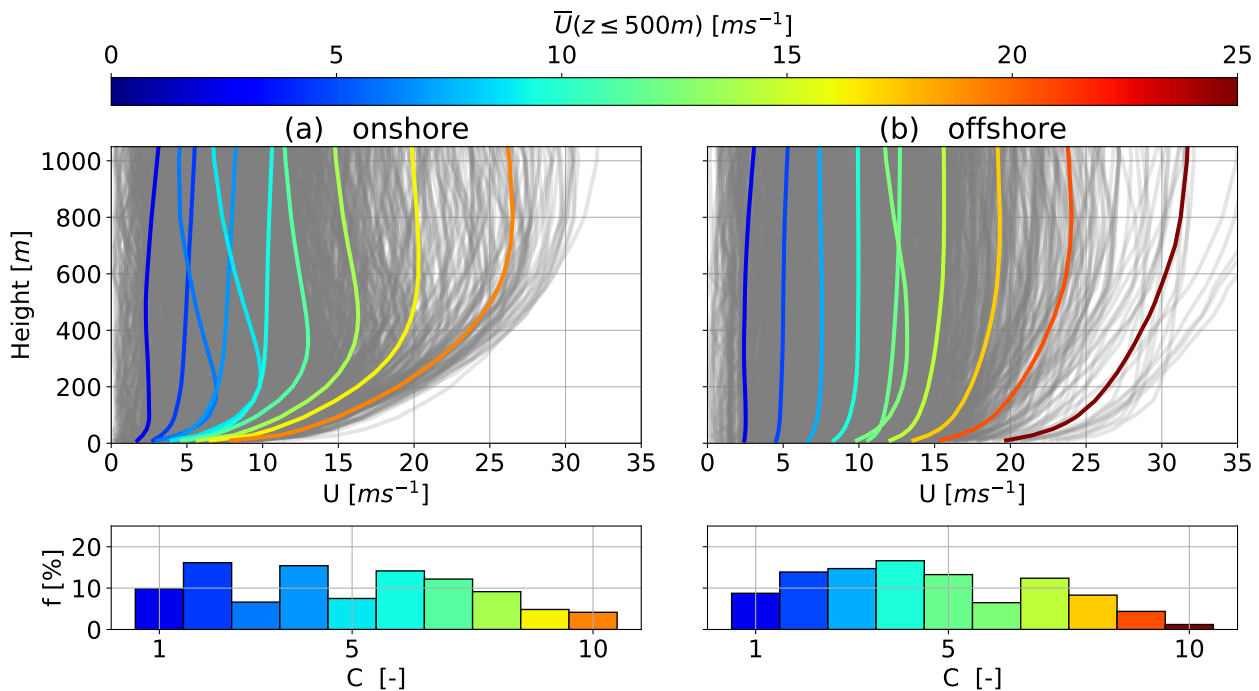


Figure 6. Onshore (left) and offshore (right) average annual wind speed profiles (or centroids) resulting from the k-means clustering process for $k = 10$ over height (top). Comprising WRF simulated wind velocity profiles depicted in grey. Centroids are sorted, labeled and colored in ascending order of average wind speed up to 500 m. The corresponding cluster frequency f for each cluster C is shown below. [remade this figure with u,v stacked. as a result different means & distribution](#)

nose at about 200 m, occurs about 5% of the time. Onshore centroids 7 and 8 also show a slight wind [speed shear](#) inversion at
 255 higher altitudes.

Evidently, the wind speed magnitude plays a [determining dominant](#) role in clustering as the resulting centroids are nearly
[stacked ordered](#) in terms of speed, especially offshore. This can lead to profiles whose shape significantly differs from the
 one of the centroid to be assigned to a cluster due to similar average wind speed. A clearer wind profile shape distinction
 could have been achieved by normalizing the data before clustering it Molina-García et al. (2019); Schelbergen et al. (2020a).
 260 Normalization was deferred to simplify and clarify the clustering procedure as the focus of this manuscript is on the derivation
 and comparison of AWES power curves. With this application in mind, it is important to note that low speed profiles with
 an almost constant speed up to high altitudes add up to about 20-30 % of annual probability. This fact is often averaged out
 when [only](#) long term average wind speed profile [shapes](#) are considered [and could lead to an overestimation of wind speeds at](#)
[higher altitudes](#). AWES therefore need to be able to either operate under such low speed conditions or be able to safely land
 265 and take-off.

3.2 Analysis of clustered statistics

Figures 8 to 12 summarize the correlation between representative clusters ($k=10$) and monthly, diurnal and atmospheric stability for the onshore (top row) and offshore (bottom row) location. This reveals patterns within the data set and gives insight into the wind prevailing regime. Clusters are sorted in ascending order of centroid average wind speed up to 500 m and colored accordingly. The corresponding centroids are shown in figure 6.

Both locations follow a distinct annual pattern (see figure 8) during which profiles associated with high wind speeds increase during the winter months and profiles with low wind speeds are predominantly found in summer. The two onshore and offshore clusters associated with the highest wind speed are almost exclusively present during November to February.

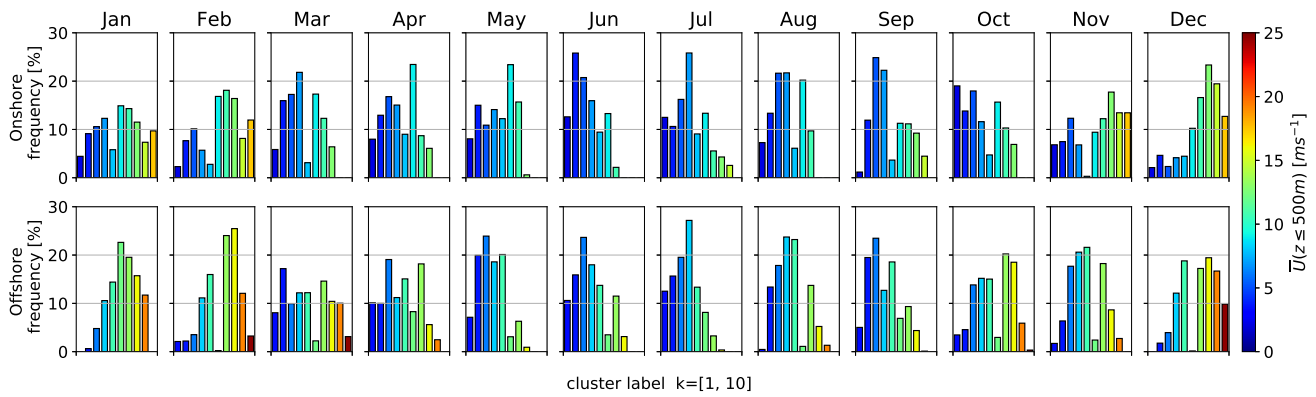


Figure 7. Monthly frequency of k-means clustered onshore (top) and (offshore) wind velocity profiles for a representative $k=10$. Clusters are sorted and colored by average wind speed up to 500 m. Centroids associated with each cluster can be found in figure 6.

Offshore data shows almost no diurnal variability (see figure 10) with only a slight increase of clusters associated with lower wind speeds during daytime. Onshore clusters on the other hand are more dependent on the diurnal cycle with a higher likelihood of low speed clusters after sunrise. The frequency of onshore cluster 5, which comprises a LLJ nose (see figure 6), drops to almost zero during daytime and increases during nighttime, substantiating the assumption that this cluster is associated with nocturnal LLJs.

The clustered wind velocity profiles and their associated speed and shape correlate with atmospheric stability as expected (see figure 12). Low wind speed clusters (~~categorized as “other” according to atmospheric stability summarized in table 2~~) ~~have a low impact on wind power assessment, but highly influence AEP because they~~ make up about 20% to 30% of the annual wind resource. These clusters exhibit Obukhov lengths close to zero (likely caused by very low friction velocity u_*) and are classified as “other” because they do not fall within one of the other atmospheric stability classes according to Floors et al. (2011) (see table 2). Unstable (U) and near unstable (NU) conditions are associated slightly higher wind speeds than “other” at both locations. The highest wind speeds develop during neutral (N) and near stable (NS) conditions. However, it should be

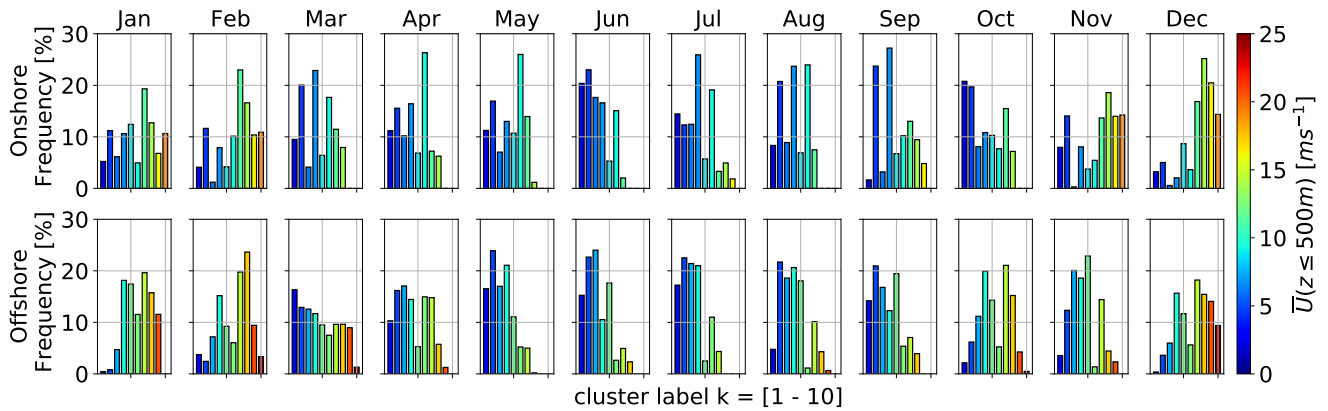


Figure 8. Monthly frequency of k-means clustered onshore (top) and (offshore) wind velocity profiles for a representative $k=10$. Clusters are sorted and colored by average wind speed up to 500 m. Centroids associated with each cluster can be found in figure 6.

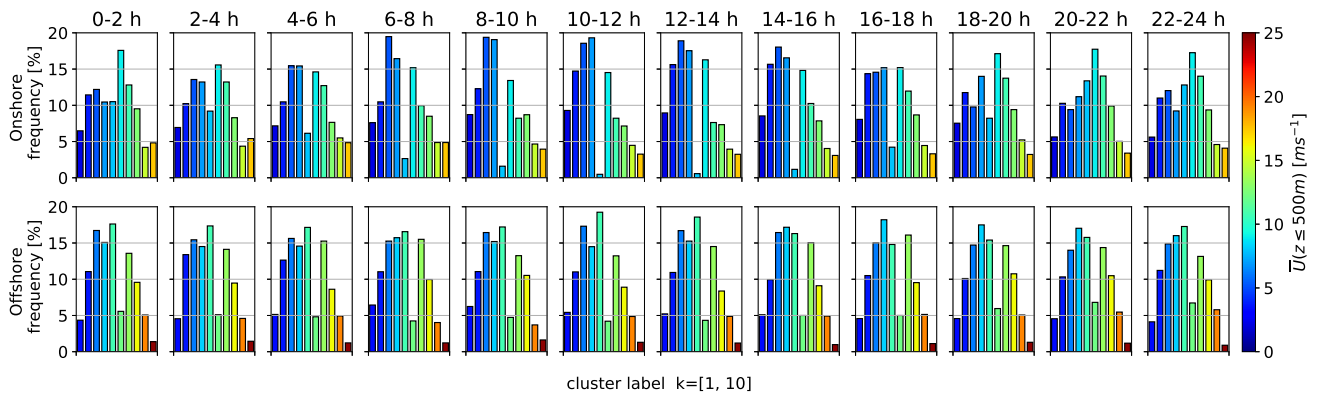


Figure 9. Diurnal frequency of k-means clustered onshore (top) and (offshore) wind velocity profiles for a representative $k=10$. Clusters are sorted and colored by average wind speed up to 500 m. Centroids associated with each cluster can be found in figure 6.

acknowledged that strong winds driven by large pressure gradients tend to drive the stratification towards neutral. LLJ profiles associated with onshore cluster 5 are most likely to develop during stable (S) and very stable (VS) conditions.

In conclusion, k-means clustering is able to capture and reveal temporal variations in the wind regime as well as location specific wind profile shapes up to high altitudes. Wind speed magnitude seems to determine the resulting clusters more than profile shape. However, less common non-monotonic profiles with LLJs were identified. Normalizing the profiles before clustering should give more insight into the different vertical profile shapes. The corresponding cluster frequency follows the expected temporal trend and atmospheric stability association.

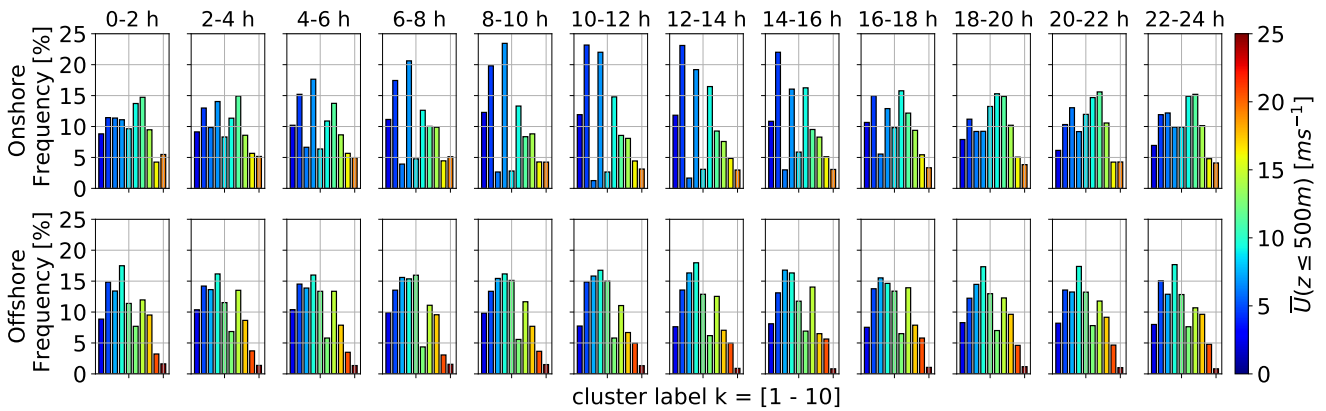


Figure 10. [new](#) Diurnal frequency of k-means clustered onshore (top) and (offshore) wind velocity profiles for a representative $k=10$. Clusters are sorted and colored by average wind speed up to 500 m. Centroids associated with each cluster can be found in figure 6.

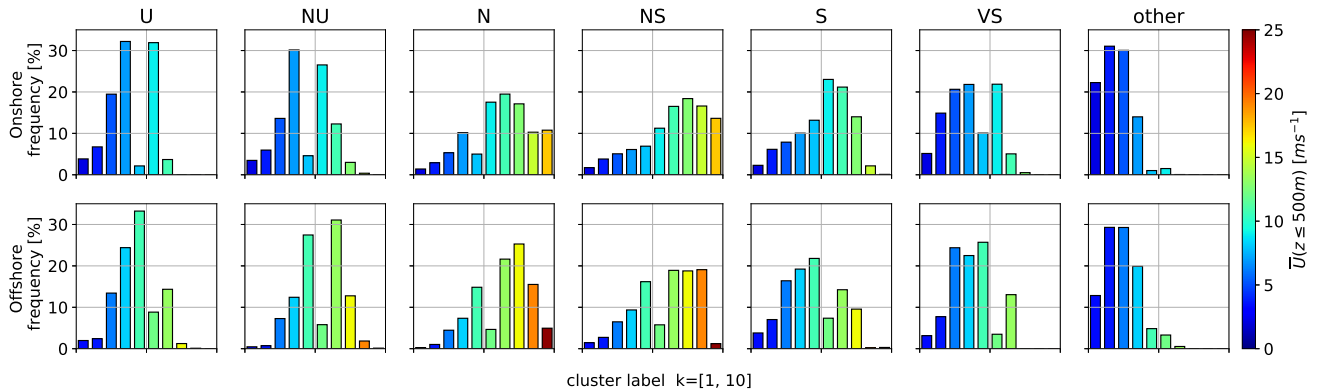


Figure 11. Atmospheric stability (U: unstable, NU: nearly unstable, N: neutral, NS: nearly stable, S: stable, VS: very stable) distribution of k-means clustered onshore (top) and (offshore) wind velocity profiles for a representative $k=10$. The associated stability classes are based on Obukhov length (see table 2). Clusters are sorted and colored by average wind speed up to 500 m. Centroids associated with each cluster can be found in figure 6.

4 AWES model

295 [This section introduced the dynamic trajectory optimization `awebox` model](#) Leuthold et al. (2020) (sub-section 4.3) and a quasi steady-state (QSS) reference ground-generation AWES model 4.1. as well as a simple steady state WT model. These models are later compared to `awebox` results in section 5. Both AWES models represent a scaled AP2 aircraft Malz et al. (2019); Ampyx (2020) [connected to a ground station via a rigid tether. All models utilize the same simulated and clustered wind speed profiles described in section 3 as boundary conditions.](#)

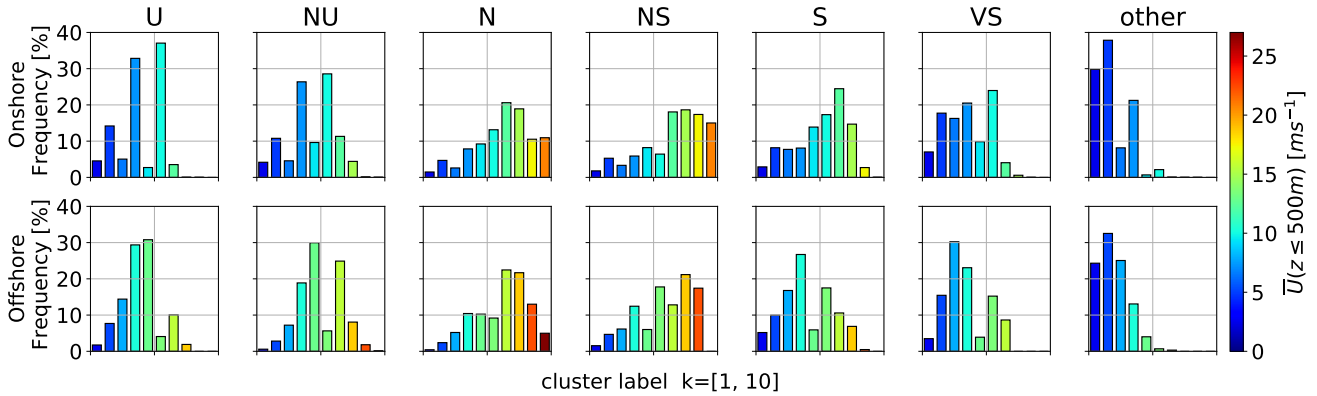


Figure 12. [new](#) Atmospheric stability (U: unstable, NU: nearly unstable, N: neutral, NS: nearly stable, S: stable, VS: very stable) distribution of k-means clustered onshore (top) and (offshore) wind velocity profiles for a representative $k=10$. The associated stability classes are based on Obukhov length (see table 2). Clusters are sorted and colored by average wind speed up to 500 m. Centroids associated with each cluster can be found in figure 6.

4.1 Engineering reference model

300 [A QSS ground-generation AWES model \(equation 2\)](#) Schmehl et al. (2013), [adapted from Loyd's crosswind power approximation](#) Loyd (1980), [describes optimal power \$P_{\text{opt}}\$ as a function of wind speed \$U\$, air density \$\rho_{\text{air}}\$ and the resultant aerodynamic force coefficient \$c_R\$ \(equation 3\). \$c_R\$ is calculated from the aerodynamic lift \$c_L\$ and total drag coefficient \$c_{D,\text{total}}\$, including tether drag. The aerodynamic coefficients and derived variables such as glide-glide ratio and \$c_R^3/c_{D,\text{total}}^2\$ can be found in section 4.4 and figure 13.](#)

$$305 \quad P_{\text{opt}} = \frac{\rho_{\text{air}}(z)}{2} A_{\text{wing}} U(z)^3 c_R \left(\frac{c_R}{c_{D,\text{total}}} \right)^2 f_{\text{opt}} (\cos \theta \cos \phi - f_{\text{opt}})^2 \quad (2)$$

$$c_R = \sqrt{c_L^2 + c_{D,\text{total}}^2} \quad (3)$$

[Aircraft and tether mass are neglected. Tether speed \$v_t\$ is non-dimensionalized in the form of the reeling factor \(\$f = \frac{v_t}{U}\$ \) with an optimal value of \$f_{\text{opt}} = \frac{1}{3} \cos \theta \cos \phi\$. The aircraft is assumed to move directly crosswind with a zero azimuth angle \$\phi = 0\$ relative to the wind direction. Elevation angle \$\theta = \arcsin\(\frac{z}{l_{\text{tether}}}\)\$ is derived from altitude \$z\$ and tether length \$l_{\text{tether}}\$. The](#)

310 [total drag coefficient \$c_{D,\text{total}}\$ determines the air resistance of the entire AWES in crosswind motion. It highly depends on the tether diameter \$d_{\text{tether}}\$ and length \$l_{\text{tether}}\$, as well as the aircraft area \$A_{\text{wing}}\$ and its aerodynamic drag coefficient \$c_{D,\text{wing}}\$ defined by the wing shape. Tether diameter \$D_{\text{tether}} = 7.8\text{mm}\$ is chosen such that rated wind speed is achieved at \$v_{\text{rated}} = 10\text{ms}^{-1}\$ \(table 3\). Figure 19 includes the QSS power curve which is defined by a combination of wind speed profile, tether length and operating height. We assume that the AWES flies at optimal power up to rated wind speed the maximum power. Beyond](#)

315 rated wind speed, power is capped at $P_{\text{rated}} = 260\text{kW}$ and tether length and operating height are adjusted to stay within this constraint. Furthermore, figure 19 shows a simple WT model (equation 9) for reference.

$$P_{\text{WT}} = c_p^{\text{WT}} \frac{1}{2} \rho_{\text{air}} A_{\text{WT}} U^3 (z_{\text{WT}} = 100 \text{ m}) \quad (4)$$

320 Hub height z_{WT} is assumed to be 100 m for both onshore and offshore WT. Rotor diameter $D_{\text{WT}} \approx 35\text{m}$ and swept area of the turbine $A_{\text{WT}} \approx 1425\text{m}^2$ (table 4) is chosen such that rated power, at a rated wind speed of $v_{\text{rated}} = 10\text{m/s}$, is equivalent to AWES rated power $P_{\text{rated}} = 260\text{kW}$, assuming a constant power coefficient of $c_p^{\text{WT}} = 0.45$.

4.2 Aerodynamic model

325 This analysis utilizes the Ampyx AP2³ Malz et al. (2019); Ampyx (2020). Aspect ratio is kept constant $AR = 10$. The total drag coefficient $c_{\text{D},\text{total}}$ highly depends on tether drag and therefore diameter d_{tether} and length l_{tether} , as well as the wing area A_{wing} and the aerodynamic drag coefficient of the wing $c_{\text{D},\text{wing}}$. We consider a straight, cylindrical tether with constant diameter and an aerodynamic tether drag coefficient $c_{\text{D},\text{tether}}$ of 1.0, which could even be higher for braided tethers. Assuming a uniform wind, the line integral along the tether results in a total effective drag coefficient of Houska and Diehl (2007); Argatov and Silvennoinen (2013); van der Vlugt et al. (2019):

$$c_{\text{D},\text{total}} = c_{\text{D},\text{wing}} + \frac{1}{4} \frac{d_{\text{tether}} l_{\text{tether}}}{A_{\text{wing}}} c_{\text{D},\text{tether}} \quad (5)$$

330 Figure 13 depicts the effect of tether drag on the $A_{\text{wing}} = 20\text{m}^2$ scaled AP2 aircraft for tether lengths up to $l_{\text{tether}} = 1000\text{m}$. Lift (a) and pitch moment (c) are assumed to behave linearly, while changes in the drag coefficient (b) are approximated quadratically. Tether drag is independent of aircraft angle of attack and therefore added to the zero-lift drag coefficient $c_{\text{D}0}$. Glide ratio $c_L/c_{\text{D},\text{total}}$ (e) and Loyd power factor $c_R^3/c_{\text{D},\text{total}}^2$ Loyd (1980) (f) not only decrease significantly with tether length, but optimal values move towards higher angle of attack. This effect will be less pronounced for larger wings due to beneficial scaling effects.

335 4.3 Dynamic optimization model

340 AWES need to dynamically adapt to changing wind conditions to optimize power generation. This can be formulated as a trajectory optimization problem which combines the interaction between tether, flying wing and ground station. For the purposes of this study, we analyze the mechanical power produced by a single tethered aircraft and assume a straight, rigid tether. Generating dynamically feasible and power-optimal AWES flight trajectories for given wind profiles is a nontrivial task given the nonlinear and unstable system dynamics and the presence of nonlinear flight envelope constraints. Optimal control

³Aerodynamic coefficients can be found under: https://github.com/awebox/awebox/blob/develop/awebox/opts/kite_data/ampyx_data.py aircraft aerodynamic model

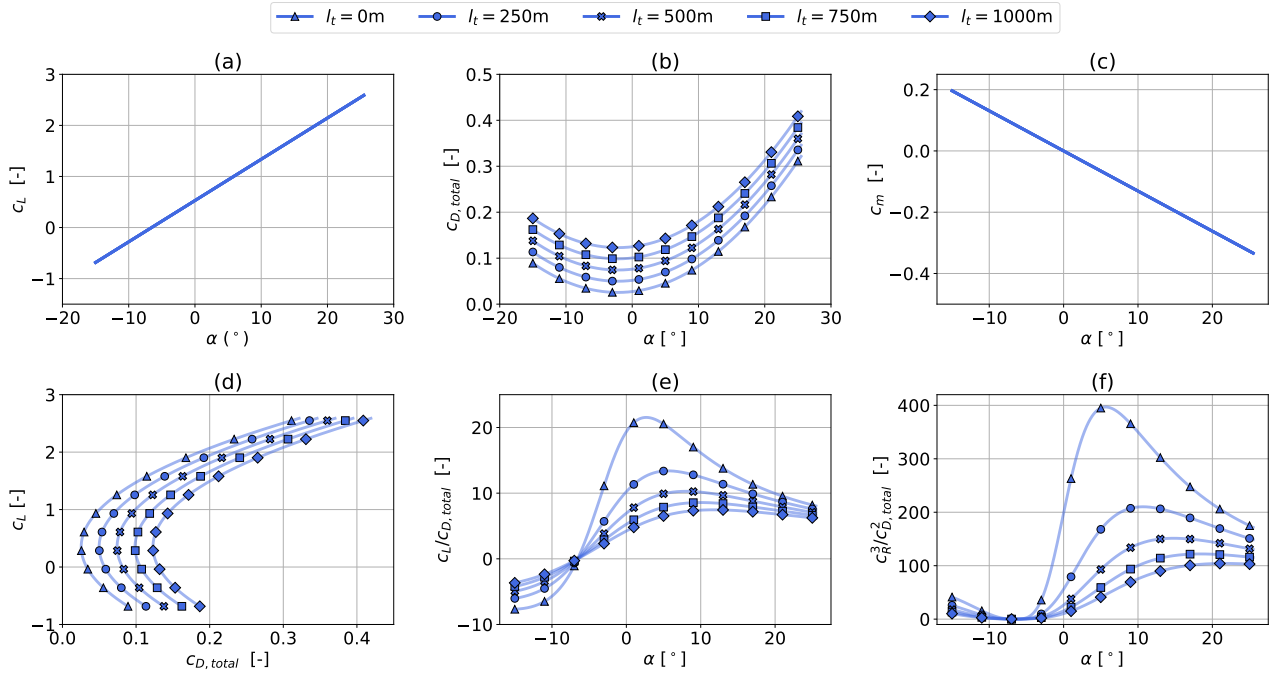


Figure 13. [Ampyx AP2 reference wing aerodynamic lift \$c_L\$ \(a\) and drag \$c_{D,total}\$ coefficients \(b\)](#) Malz et al. (2019); Ampyx (2020), [including tether drag according to equation 5, for a wing area \$A_{wing}\$ of \$20m^2\$ and tether diameter of \$D_{tether} = 7.8mm\$ \(see table 3. Tether length varies between 250 m and 1000 m. \(c\) shows the pitch moment coefficient \$c_m\$ as a function of angle of attack. The bottom figures display lift over drag \(d\), lift to drag ratio over angle of attack \(e\) and \$c_L^3/c_{D,total}^2\$ over angle of attack according to Loyd Loyd \(1980\).](#)

methods are a natural candidate to tackle this problem, given their inherent ability to deal with nonlinear, constrained multiple-input-multiple-output systems. In periodic optimal control, an optimization problem is solved to compute periodic system state and control trajectories that optimize a system performance index (here average AWES power output \bar{P}) while satisfying the system dynamic equations. The initial and final state of the trajectory are freely chosen by the optimizer but must be equal to ensure periodic operation. We here apply this methodology to generate realistic single-wing, ground-generation AWES power curves and AEP estimation based on [WRF-simulated wind velocity profiles using the `awebbox`](#). Take-off and landing are not considered in this paper. Instead, only the production cycle, including reel-out as well as reel-in period, is optimized.

We consider a 6 degree of freedom (DOF) rigid-wing aircraft model [which is connected to the ground via a rigid tether, thereby reducing the DOF to 5](#). It uses pre-computed quadratic approximations of the aerodynamic coefficients which are controlled via aileron, elevator and rudder deflection rates Malz et al. (2019). The tether is controlled by the tether jerk $\ddot{\dot{l}}_{tether}$ from which tether acceleration \ddot{l}_{tether} , speed $\dot{l}_{tether} = v_{tether}$ and length (l_{tether}) are derived. The tether is modeled as a single solid rod which can not be subjected to compressive forces De Schutter et al. (2019). The rod is divided into $n_{aero} = 10$ elements and tether drag is calculated individually for each element relative to apparent wind speed Bronnenmeyer (2018),

with a tether drag coefficient of $c_D^{\text{tether}} = 1$. Wind profiles are implemented as 2D wind components rotated such that the main
 355 wind direction (u_{main} as defined by the average wind direction up to 500 m, compare section 3) is in positive x direction and
 the deviation from it in y direction. This is equivalent to assuming omnidirectional AWES operation with the wing still needing
 to adjust to changing wind conditions with height. **Ref2: I'm curious about how pressure & density vary with stable vs.
 unstable conditions and how much that affects power. Markus: Not considered** Furthermore, we include a simplified
 atmospheric model based on international standard atmosphere to account for air density variation.

360 4.4 Aircraft model

The aircraft aerodynamic coefficients are those available for the Ampyx AP2 for comparison with other publications and since
 no other AWES data were available. Figure 14 (left) visualizes the implemented aircraft lift c_L and drag coefficient c_D .

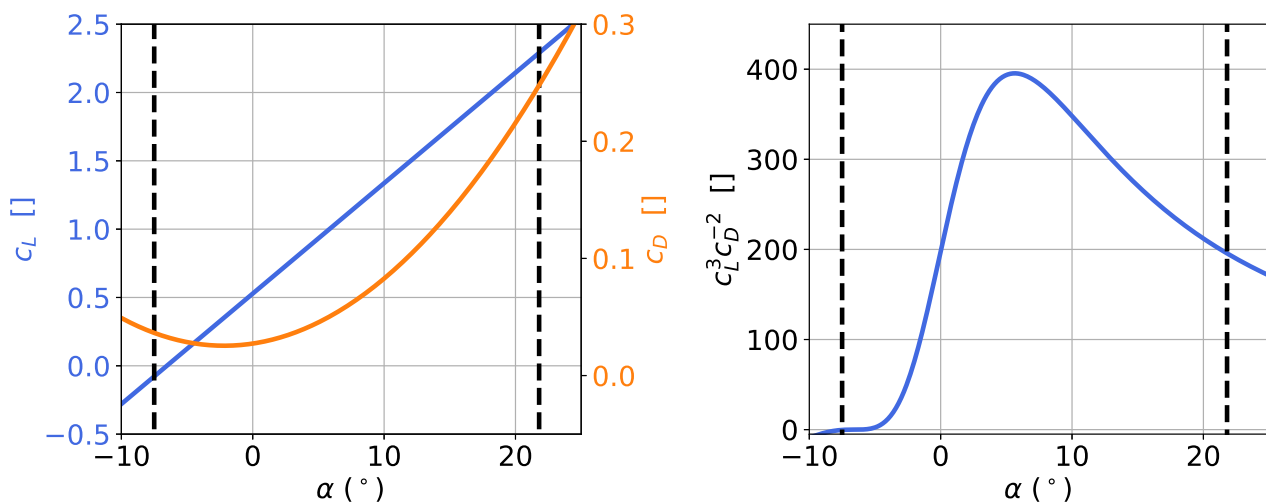


Figure 14. Left: dimensionless Ampyx AP2 Malz et al. (2019); Ampyx (2020), lift c_L and drag coefficients c_D over angle of attack α used in this study. Vertical dashed black lines visualize the angle of attack constraints. Right: c_L^3/c_D^2 according to Loyd Loyd (1980) over angle of attack α . Vertical dashed black lines visualize the angle of attack constraints.

Lift is assumed to behave linearly in between the angle of attack constraints, visualized by black, vertical, dashed lines. Changes in the drag coefficient on the other hand are implemented by a quadratic approximation. This study compares two
 365 aircraft sizes, one with a wing area of $A = 20 \text{ m}^2$ and another one with $A = 50 \text{ m}^2$. Aircraft geometry such as aspect ratio is kept constant ($AR = 10$). The Aircraft mass m and inertia J are scaled relative to wing span b with a mass scaling exponent κ (see equation 6), based on Galileo's square-cube law.

$$m_{\text{scaled}} = m_{\text{ref}} \left(\frac{b}{b_{\text{ref}}} \right)^\kappa ; \quad J_{\text{scaled}} = J_{\text{ref}} \left(\frac{b}{b_{\text{ref}}} \right)^{\kappa+2} \quad (6)$$

370 Pure geometric scaling corresponds to $\kappa = 3$, but in reality, as has been seen for conventional WT, design and material improvements occur with scaling over time. A review of the available literature containing system mass details was conducted to identify an appropriate mass scaling factor. The results are shown in 15. Actual and anticipated AWES scale with a $\kappa = 2.2 - 2.6$ (grey area). Based on a curve fit to the available published sizing study data, $\kappa = 2.4$ seems reasonable for future AWES development, but we leave a fulsome system AWES scaling study to future work. It can be assumed that lighter aircraft result in a lower cut-in wind speeds and higher power output. However, we chose a rather optimistic κ of 2 (pure geometric scaling would assume $\kappa = 3$), assuming design and material improvements with scale. Assuming such a low mass scaling exponent is unrealistic and will be changed to 2.7 in the published paper.

375 ~~geometric scaling would assume $\kappa = 3$), assuming design and material improvements with scale. Assuming such a low mass scaling exponent is unrealistic and will be changed to 2.7 in the published paper.~~

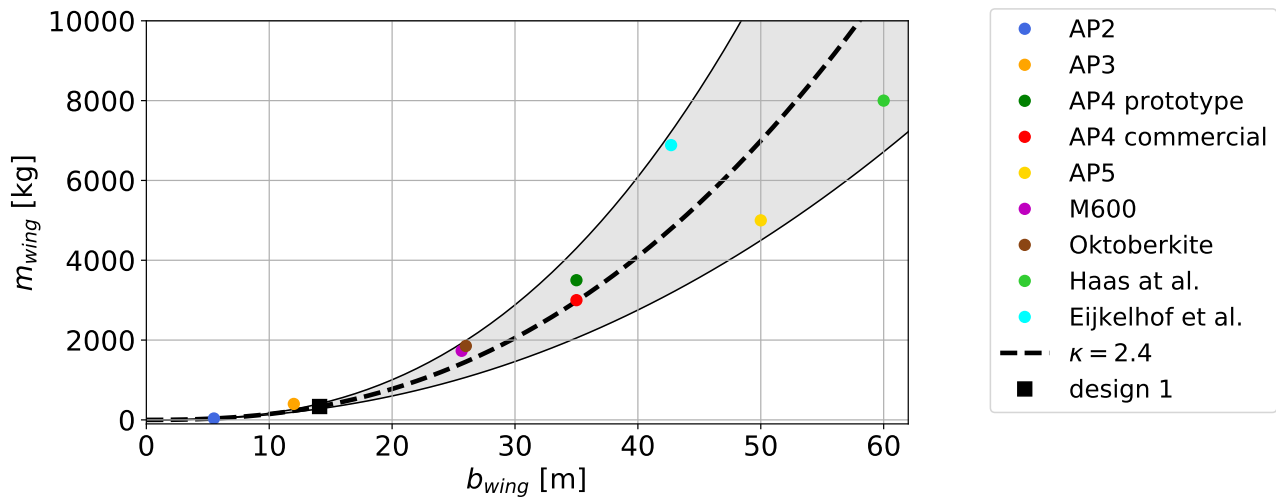


Figure 15. Curve fit of published sizing study AWES aircraft mass Haas et al. (2019); Kruijff and Ruiterskamp (2018); Eijkelhof et al. (2020); Ampyx (2020); Echeverri et al. (2020). For these data mass scales within a scaling exponent range of $\kappa = 2.2 - 2.6$ (grey area). The chosen mass scaling exponent of $\kappa = 2.4$ is represented by a dashed line and the modeled design is highlighted by a black square.

~~The wing loading of approximately 12.25 kgm^{-2} is consistent with the AP2 reference data. This results in an overestimation of output power and lower cut-in speed in comparison to a heavier aircraft. The focus of this paper is on the derivation and investigation of the AWES power curve and not on realistic system design which will be subject of a future paper on scaling study of AWES.~~

380 ~~study of AWES.~~

According to Loyd Loyd (1980) the ratio c_L^3/c_D^2 determines the maximum power of crosswind AWES. Figure 14 (right) only gives a rough estimate of optimal reel-out phase angle of attack α , as tether drag is not included here. Including tether drag greatly reduces total system $c_L^3/c_{D,\text{total}}^2$ and shifts the optimal angle of attack of the wing towards higher values. Figures 13 and ?? show AP2 and HL aerodynamic coefficients for various tether diameters, including a simplified tether drag model. The resulting optimal power and operating altitude, estimated based on a QSS engineering model, are found in chapter ??.

385 ~~resulting optimal power and operating altitude, estimated based on a QSS engineering model, are found in chapter ??.~~

Table 3. Aircraft design parameters for AWES $A_{\text{wing}} = 20 \text{ m}^2$ analyzed in this study and for the original AP2 aircraft. Values in square brackets represent flight envelope bounds, which are implemented as inequality constraints of the optimization.

	Parameter	AP2	design 1
Aircraft	wing area [m^2]	3	20
	wing chord [m]	0.55	1.42
	wing span [m]	5.5	14.1
	wing AR [-]	10	10
	kite mass [kg]	36.8	355
	β [$^\circ$]		[-15 : 15]
Tether	max. length [m]		2000
	speed [ms^{-1}]		[-15 : 10]
	max. acceleration [ms^{-2}]		[-10 : 10]
	diameter [mm]		<u>7.8</u>
	max. stress [Pa]		$3.6 \cdot 10^9$
	max. force [kN]		60
	min operating altitude [m]		60

4.5 Ground station model

The ground station is not explicitly modeled in our investigation, but implemented as a set of constraints which ~~The ground station constraints~~ play a decisive role in the generated power of ground-generation AWES. The optimal reel-out speed is $v_{\text{out}} \approx \frac{1}{3} v_{\text{wind}}$ Loyd (1980) ~~and thereby limited by the prevailing wind conditions which hardly exceed 20 ms^{-1} . ,thereby the~~ reel-out speed is expected to remain below 10 ms^{-1} as the wind speed hardly exceeds 20 ms^{-1} . ~~The reel-out to reel-in ratio is limited to $\frac{2}{3}$, e.g. $\frac{v_{\text{out}}}{v_{\text{in}}} = \frac{10 \text{ ms}^{-1}}{15 \text{ ms}^{-1}}$, to comply with ground station design limitations. A reel-out speed of $v_{\text{out}} = 15 \text{ ms}^{-1}$ and reel-in speed of $v_{\text{out}} = 10 \text{ ms}^{-1}$ were chosen, resulting in a reel-out to reel-in ratio of $\frac{2}{3}$ which is assumed to be within design limitations.~~ A maximum tether acceleration of $\ddot{l} = 20 \text{ ms}^{-2}$ is imposed to comply with generator torque limits. ~~Tether diameter and maximum tether force are calculated from a pre-optimization, due to the complexity of the system which makes an a priori estimation difficult. This calculation optimizes the AWES trajectory and tether diameter to maximize average cycle power subject to the same tether speed and acceleration constraint. A simple logarithmic wind speed profile was used as wind inflow (reference speed of $U_{\text{sizing}}(z=10 \text{ m}) = 8 \text{ ms}^{-1}$). The tether diameter is chosen such that rated power is achieved at $U_{\text{ref}} = 10 \text{ ms}^{-1}$~~ Constraints on the tether force enforce it to be positive whilst not exceeding the maximum tether stress, to which a safety factor of 3 is applied. This results in a tripling of the cross-sectional tether area. These ground station and tether

constraints do not represent an optimized AWES, but rather a representative system.

4.6 Constraints

The tether constraints such as tether length, speed and force are summarized in table 3 (see sub-section 4.5). Flight envelope constraints include ~~limits on~~ limitation of aircraft acceleration, roll and pitch angle (to avoid collision with the tether) ~~or~~ and angle of attack. ~~in-between-which-the~~ The lift coefficient is assumed to be linear within this range. Furthermore, a minimal operating height of $z_{\min} = 50 + \frac{A_{\text{wing}}}{2}$ m is imposed for safety reasons.

4.7 Wind boundary condition

AWES trajectories depend on prevailing wind conditions as they greatly benefit from dynamically continuously adapting their operational altitude, tether speed and path to maximize power production and minimize losses. The above described AWESs were subjected to several different wind conditions to compare the impact on their trajectory, estimate the power curve and AEP. Logarithmic wind speed profiles (equation 7) with a roughness length of $z_0^{\text{onshore}} = 0.1$ and $z_0^{\text{offshore}} = 0.001$ are used as reference because they are the standard of wind energy industry. A standard Rayleigh distribution with $U_{\text{ave}}^{\text{onshore}} = 10 \text{ ms}^{-1}$ and $U_{\text{ave}}^{\text{offshore}} = 12 \text{ ms}^{-1}$ is used to estimate AEP (sub-sections 5.3, 5.4) International Electrotechnical Commission (2010).

$$U_{\log} = U_{\text{ref}} \left(\frac{\log_{10}(z/z_0)}{\log_{10}(z_{\text{ref}}/z_0)} \right) \quad (7)$$

The reference wind speed U_{ref} at reference height $z_{\text{ref}} = 10$ m was varied from 3 to 19 ms^{-1} in steps of $\Delta U_{\text{ref}} = 2 \text{ ms}^{-1}$ to cover more than the common wind speed range. Results are compared to clustered, WRF simulated, onshore and offshore wind conditions in terms of power curve and AEP. We assume the same wind speed probability distribution for WRF wind profiles as well as the logarithmic reference wind speed profiles. Within each cluster, three WRF-calculated wind velocity profiles were chosen to assess the AWES power curve. Based on the average wind speed up to 500 m, which is used as a proxy for operating height ranges, the 5th, 50th and 95th percentile profile are chosen to represent the spectrum of wind conditions within each cluster. ~~with a p-value of 5,50, 95, based on average wind speed up to 500 m within every cluster, were chosen to assess the AWES power curve. A representative k=20 is a reasonable choice according to the elbow method and silhouette score described in section 3.~~ Analyses on AWES performance (section 5) and power curve estimation (section 5.3) are based on k=20 clusters with 3 wind profiles per cluster, a reasonable choice in terms of computational cost, representation of wind conditions and clustering quality (see section 3) ~~To estimate AEP,~~ Cluster centroids across the range of $k = 5 - 100$ were implemented to estimate AEP. Wind conditions for the AEP estimation are based on the cluster centroids for $k = 5 - 100$ due to the high computational cost of running multiple profiles per cluster. These results are compared to the AEP calculated from power of k=20 p5, p50 and p95 wind profiles.

4.8 Problem formulation and solution

AWES trajectory optimization is a highly nonlinear and non-convex problem which likely has multiple local optima. Therefore, the particular results generated by a numerical optimization solver can only guaranty local optimality, and usually depend on

the chosen initialization. This can result in unwanted or unrealistic AWES trajectories, which implies that the quality of all solutions needs to be evaluated a posteriori.

A periodic optimal control problem is formulated to maximize the average cycle power \bar{P} of a single AWES subject to equality (e.g. tether diameter) and inequality constraints described above De Schutter et al. (2019); Leuthold et al. (2018). The trajectory optimization problem is discretized into 100 intervals using direct collocation.

An initial guess is generated using a homotopy technique similar to Gros et al. (2013). ~~with an A estimated~~ circular trajectory ~~is estimated~~ based on a fixed number of loops (here $n_{loop} = 5$) at a ~~30° 15°~~ elevation angle ~~and the initial tether length. Initial aircraft speed is based on the estimated duration of a single loop (here 10 sec) an estimated aircraft speed.~~ Previous analyses showed that the `awebbox`-estimated power output is insensitive to the number of loops and therefore flight time, at least for less than 10 loops. The homotopy technique initially fully relaxes the dynamic constraints using fictitious forces and moments to reduce model nonlinearity and coupling, improving the convergence of Newton-type optimization techniques. The constraints are then gradually re-introduced until the relaxed problem matches the original problem. The resulting nonlinear program (NLP) is formulated in the symbolic modeling framework CasADi for Python Andersson et al. (2019) and solved using the linear solver MA57 HSL (2020) in IPOPT Wächter and Biegler (2006).

445 5 Results

In this section we compare AWES trajectories and time series trends based on representative onshore (Pritzwalk) and offshore (FINO3) wind conditions. Building on that onshore and offshore operating height statistics and tether length trends are examined. AWES power curves are determined based on average cycle power and wind speeds at different reference heights. A quasi-steady reference AWES model (described in sub-section 4.1) as well as a WT model contextualize the results. ~~From these power curve trends we determine an AWES power coefficient c_p^{AWES} similar to conventional WT to allow for a quick estimate of AWES power based on wing area, path length and wind speed.~~ Lastly, we compare performance in terms of annual energy production (AEP) and capacity factor (cf) estimates for different number of clusters and reference heights. ~~of different number of clusters are compared to Rayleigh distributed log-profiles as they are defined by IEC standards.~~

5.1 Flight trajectory and time series results

445 This sub-section offers insight into typical optimized AWES flight trajectories. Figures 16 and A2 (appendix) compare the trajectories of representative ~~(chosen because of different wind speeds and profile shape)~~ onshore and offshore profiles wind conditions between typical low and high wind speeds for an aircraft with a wing area of $A_{wing} = 20 \text{ m}^2$. ~~Results for an aircraft with a wing area of 50 m^2 can be found in the appendix (see figures A2).~~

The top left sub-figure in figure 16 and A2 show the wind speed profiles U over altitude z with the operating height highlighted in color. The colored segments also depict the Lagrange polynomials that interpolate the WRF simulation data for optimization purposes. ~~Note that wind speed profiles (magnitude) are depicted here instead of wind velocity profiles (rotated horizontal u_{main} and $u_{deviation}$ wind component) for readability purposes.~~ The bottom left figure shows a top view of the

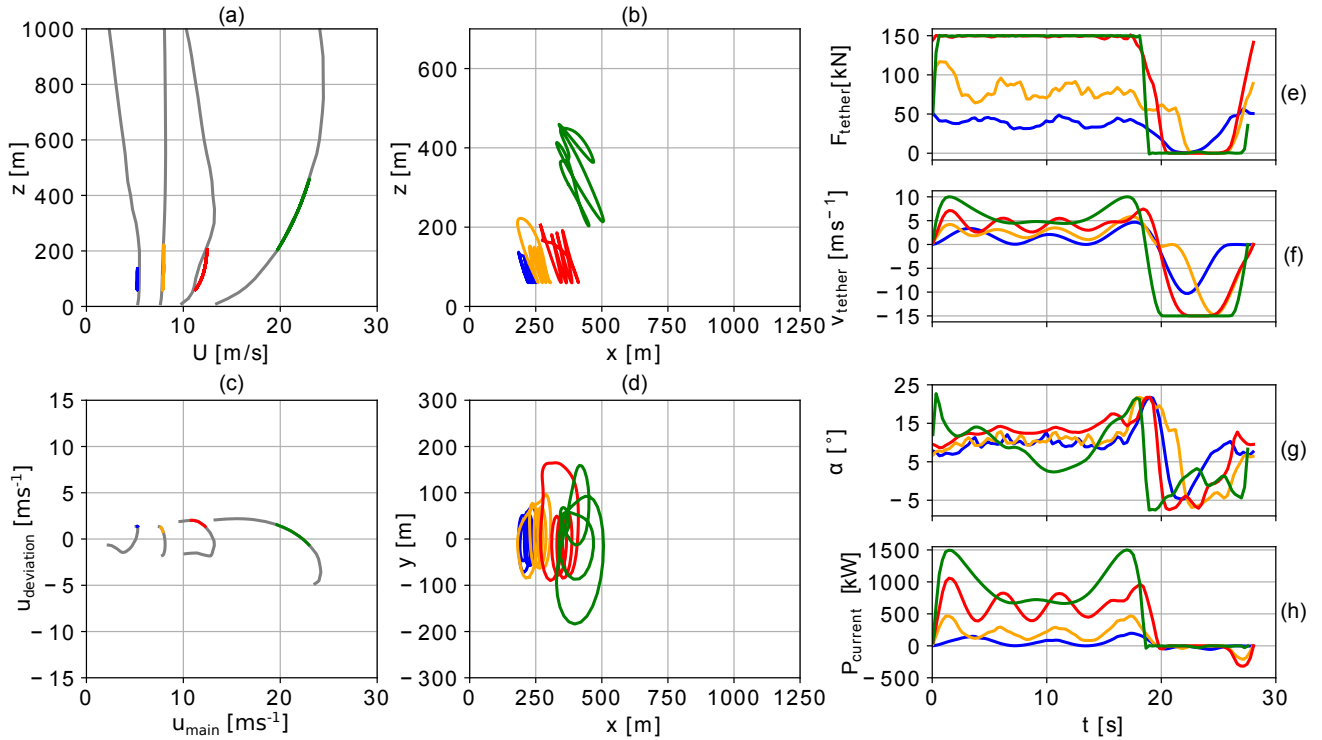


Figure 16. Representative wind speed profiles (left top), and hodograph (top view) of wind velocity up to 1000 m (left bottom). [Wind profiles](#) chosen to represent typical low (blue, orange), medium (red) and high wind speeds (green). ~~The deviation of the colored lines is caused by the approximation of discrete data points with Lagrange polynomials.~~ Trajectories (center) in side and top view. Temporal variations of tether force F_{tether} (right 1st from top), tether speed v_{tether} (right 2nd from top), angle of attack α (right 3rd from top) and instantaneous power P_{current} (right, bottom) optimized based on clustered onshore wind speed profiles for a ground-generation AWES with a wing area of $A_{\text{wing}} = 20 \text{ m}^2$ [changed u and v to \$u_{\text{main}}\$ and \$u_{\text{deviation}}\$.](#)

wind velocity profile (rotated horizontal u_{main} and $u_{\text{deviation}}$ wind component) in grey up to 1000 m displayed above as well as ~~the wind velocity components as experienced by the AWES in color.~~ [the part of the profiles corresponding to the height range swept by the aircraft in color.](#) ~~As expected based on theory~~ Stull (1988) ~~and from the wind rose in section 2.2, the onshore profiles veer more than offshore profiles.~~ The two center plots show the optimized trajectory in side view (center top, x-yz plane) and top view (center bottom, x-y plane).

When maximum tether force is reached the system starts to de-power while maintaining the same high tension (right, 1st from top in figures 16 and A2). Such trajectories often extend perpendicular to the main wind direction (~~y-direction~~). This often results in odd ~~and unrealistic~~ or unexpected trajectories, even though these local minima are within the system constraints (roll rate etc.). De-powering by increasing the elevation angle is also possible and likely to happen, but harder to determine as it is not easily identifiable whether the elevation angle increased due to better wind conditions or to de-power the wing. Reducing

the angle of attack (right, 3rd from top) while maintaining constant maximum tether force (right, 1st from top) can be observed in the highest onshore wind speed trajectory (green). During the production loops, the angle of attack constraint of the red and orange trajectories are active. The AWES angle of attack at the onshore location is generally higher than offshore (compare the third sub-figure on the right in figure 16 and A2). This can likely be attributed to the fact that onshore tether lengths are generally longer than offshore, where beneficial wind conditions allow the AWES to operate at lower altitudes (see figure 18). As a result, the optimal c_L^3/c_D^2 shifts towards higher angle of attack.

The algorithm seems to always maximize tether force and vary tether speed (right 2nd from top) close to optimal reel-out speed ($v_{out} \approx \frac{1}{3} v_{wind}$ Loyd (1980)) to maximize average cycle power. At high wind speeds the tether speed constraint is active during the reel-in phase, presumably to keep this phase as short as possible. In these cases the trajectory starts to differ from its predefined shape with distinct loops to and the system de-powers, visible in which can be seen in the power development during the production phase (green). Trajectories for such high speed wind conditions without a tether force constraint, where the tether diameter is adjusted to the wind conditions, would be closer to the looping paths seen for lower wind speeds (blue, orange, red). The optimizer tries to keep the reel-in phase as short as possible, given tether speed and acceleration constraints. As a result, the reel-in tether speed reaches its limit for high wind speeds. The time history of instantaneous power $P_{current}$ (right bottom) clearly distinguishes the production and consumption phase of pumping-mode (ground-generation) AWES. However, all optimized trajectories have a close to zero power usage during reel-in as they reduce the angle of attack to near zero lift conditions. One commonality between all time series is that they all almost have the same flight time independent of location, wind speed or aircraft size. The flight time is almost solely determined by the initial number of loops, here five, used in the initialization procedure. Based on previous analyses, mechanical AWES power output seems to be insensitive to number of loops and flight time. The optimized trajectories result in almost zero tether force and therefore energy consumption during the reel-in phase. This might be different for real deployment, where higher number of loops could be more beneficial, because the reel-in time relative to reel-out time could be shorter. Ref2: I'd address elevation angle here; based on figure 10, it looks like the optimizer found a common optimal elevation angle for several of the cases, which links tether length and altitude. Vander Lind 2013 calculated an optimal elevation angle for fly-gen systems assuming an exponential wind profile; I'm curious how close this elevation angle is. Makrus: Rather include in next subsection & in stats

5.2 Tether length and altitude

This sub-section compares tether lengths and operating altitudes for onshore and offshore wind conditions for a wing size of $A_{wing} = 20 \text{ m}^2$. Results for the $A_{wing} = 50 \text{ m}^2$ design can be found in the appendix in figure A3. The data is based on the p5, p50, p95-th wind profiles of k=20 onshore and offshore clusters (see sub-section 4.7).

Figure 18 (left) illustrates the minimum (blue) and maximum (orange) tether length l_{tether} over reference wind speed, here $U(z_{ref} = 200 \text{ m})$, for both onshore (top a) and offshore (bottom c). Similar results derived from the quasi steady-state engineering model (equation 2), including losses associated with elevation angle and tether drag, can be found in chapter ??. Figures ?? and ?? show similar optimal operating altitudes between 100 and 400m. The right side of the figure shows the frequency distribution of operating altitude $z_{operating}$, calculated based on the 100 time steps per trajectory described

above in sub-section 5.1. Neither of the optimizations reaches the maximum tether length of $l_{\text{tether}}^{\text{max}} = 2000$ m. Generally, tether length increases with wind speed, but comparing both locations two very different trends emerge. Onshore, tethers are generally longer than offshore as operating altitudes tend to be higher due to higher wind shear. and typically higher winds offshore. Where a tether length of approximately 600 m suffices for the entire offshore wind regime, onshore tethers need to be at least 1000 m long, except for a few outliers which would benefit from an even longer tether. The gradual increase of tether length with wind speed offshore is probably due to lower wind shear and more homogeneous wind regime (see sub-section 2.2). Onshore tethers on the other hand already exceed a length of 400 m from $U(z_{\text{ref}} = 200 \text{ m}) > 5 \text{ ms}^{-1}$.

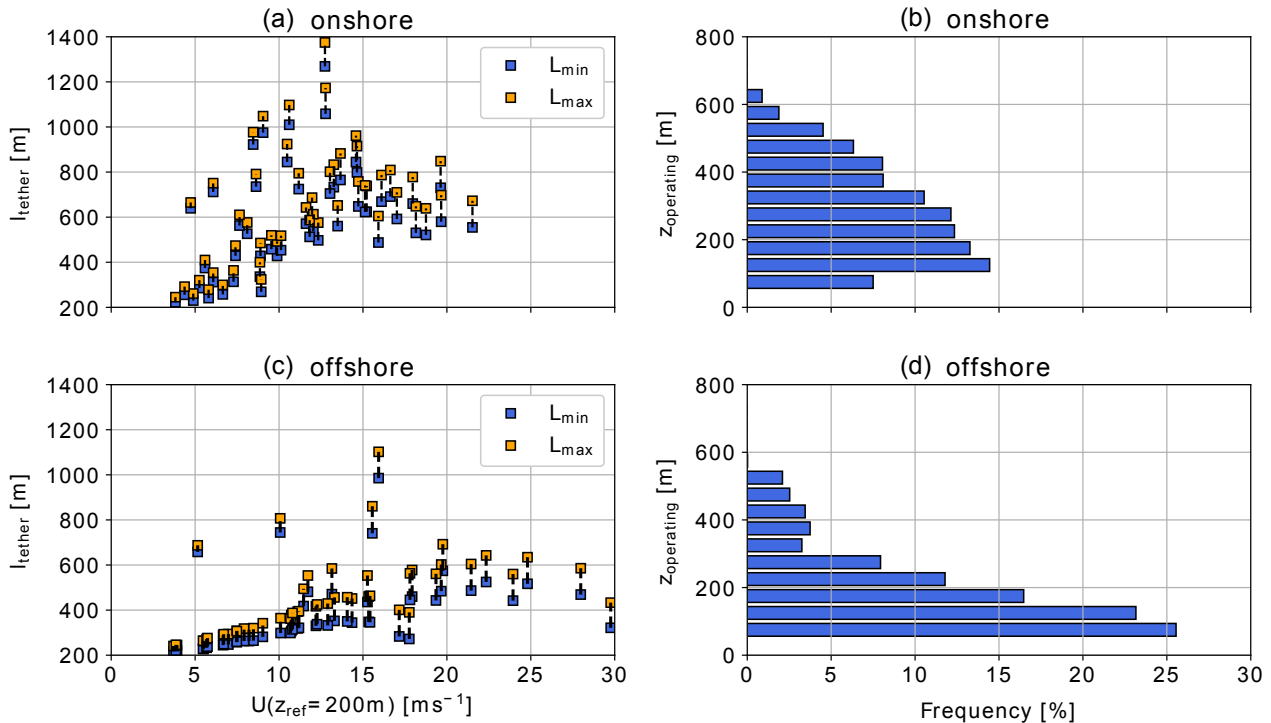


Figure 17. Tether length range (left) over reference wind speed $U(z_{\text{ref}} = 200 \text{ m})$ and frequency distribution of operating altitude (right) based on k=20 onshore (top) and offshore (bottom) clusters for a ground-generation aircraft with a wing area of $A_{\text{wing}} = 20 \text{ m}^2$.

Operating altitudes over the entire wind regime, both off- and onshore, are almost never higher than 500 m above ground, 515 confirming findings in Sommerfeld et al. (2019a, b). Low altitude offshore winds seem to be so favorable that AWES operate approximately 75% annually below 250 m. This also has implications for tower-based, conventional wind turbines as these results suggest that the benefit of going towards higher altitudes might not outweigh the costs. This is seen in large WTs, such as the IEA-15-MW reference turbine Gaertner et al. (2020), with hub height smaller than one rotor diameter. Multi-wing AWES could benefit from higher operating altitudes due to their higher lift to tether drag and weight ratio. However, more detailed 520 analysis are required. The $A_{\text{wing}} = 50 \text{ m}^2$ aircraft both on- and offshore seems to benefit from higher operating altitudes and

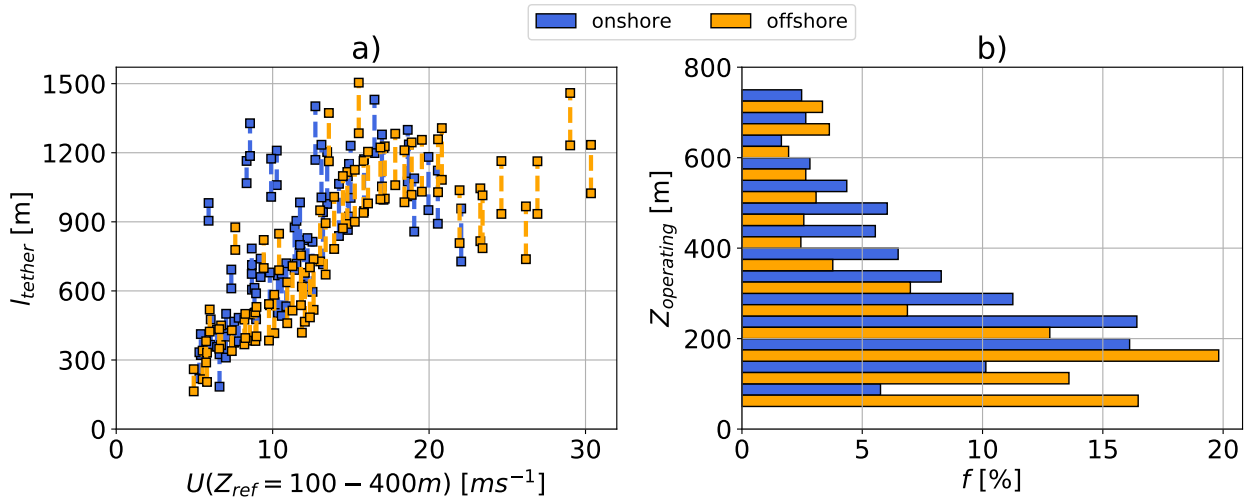


Figure 18. [New figure](#)

longer tethers (see figure A3) which could be due to the higher lift to tether drag ratio. **However,** Optimal operating altitudes [of the \$A_{wing} = 50 \text{ m}^2\$ aircraft only](#) exceed heights above 600 m at either location **only** 5% of the time. A future analysis of even larger systems will investigate whether this trend continues.

5.3 Power curve

525 [Figure 19 \(a, b\) compare dynamic optimized AWES power curves based on onshore \(blue\) and offshore \(orange\) clustered and logarithmic wind speed profiles \(dotted lines\) to the AWES QSS model \(solid line\) as well as a simplified WT model \(red line\) described in sub-section 4.1. A cut-in wind speed of \$5 \text{ m}^{-1}\$ is chosen as optimizations below this threshold did not converge. No cut-out wind speeds was defined. Therefore, energy conversion is only limited by the wind resource. The presented AWES and WT reach rated power around \$U_{ref} \approx 12 \text{ ms}^{-1}\$. Logarithmic wind speeds calculated with equation 7 and roughness lengths](#)
 530 [of \$z_0^{onshore} = 0.1\$ and \$z_0^{offshore} = 0.001\$ \(section 4.7\) With average wind speed between 100 and 400 m as reference wind speed \(abscissa\) the clustered power data form a relatively smooth power curve. This choice on the other hand results in the irregular shapes of the WT and QSS power curves. For the calculation of wind speed and energy distribution a reference height of 100m is used for the WT. Cycle-average power data points result from AWES trajectory optimizations of 3 wind velocity profiles within each of the k clusters \(here k=20\). Furthermore, the clustered power curve fit aligns well with optimization results for](#)
 535 [logarithmic wind speed profiles at this reference height.](#)

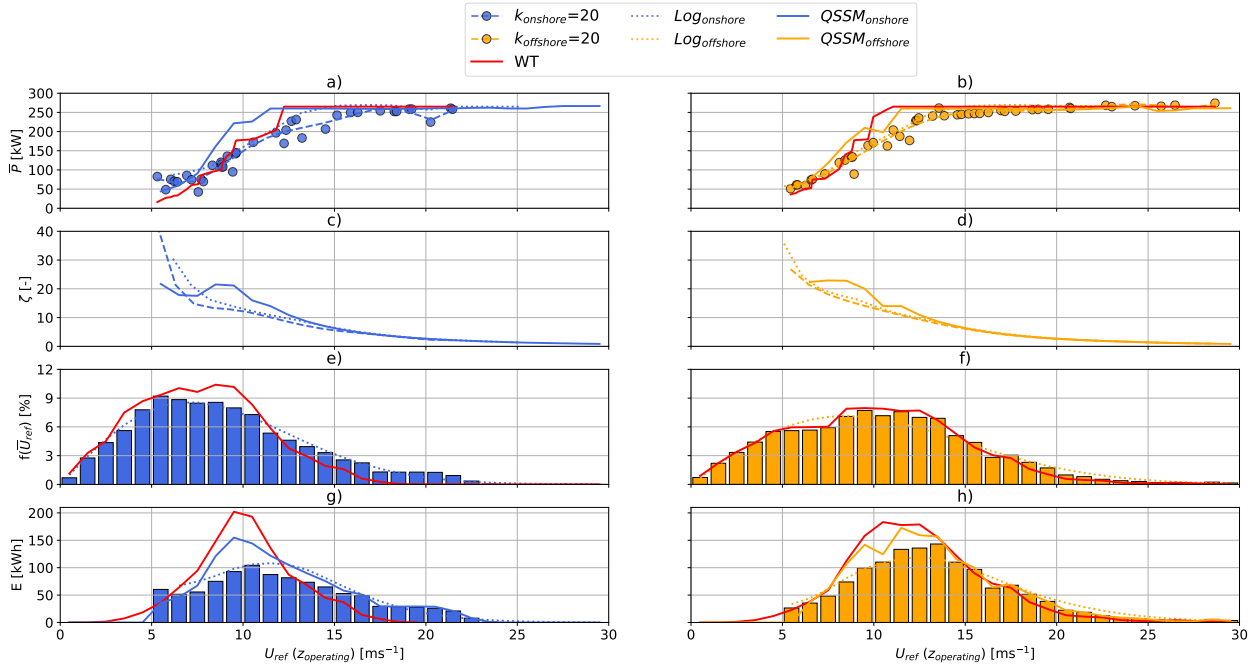


Figure 19. Onshore (blue) and offshore (orange) AWES power curves (a,b) over average wind speed between $z = 100 - 300$ m based on 3 wind profiles for each of the $k=20$ clusters. Simplified WT model (red lines), QSS AWES model (solid lines) and AWES subject to logarithmic wind boundary conditions (dotted lines) with rated wind speed of $v_{\text{rated}} = 10 \text{ m s}^{-1}$ and the same rated power for reference. Harvesting factor ζ (equation 8 shown in c, d. Annual energy distribution (e,f) based on power curves and WRF-simulated annual wind speed probability distributions (c,d) and standard Rayleigh distributions. International Electrotechnical Commission (2010).

Sub figures c and d show the AWES harvesting factor ζ Diehl (2013) which expresses the estimated AWES power P relative to the total wind power through an area the same size as the wing P_{area} . Here the reference wind speed $U_{\text{ref}}(z = 100 - 300 - \text{m})$ is used to estimate ζ .

$$\zeta = \frac{P}{P_{\text{area}}} = \frac{P}{\frac{1}{2} \rho_{\text{air}} A_{\text{wing}} U(z)^3} \leq \frac{4}{27} c_{\text{R}} \left(\frac{c_{\text{R}}}{c_{\text{D}}} \right)^2 \quad (8)$$

540 At low wind speeds the optimization model seemingly outperforms the QSS model which is likely caused by optimizer exceeding some constraints within certain tolerances. Another possible explanation is that the choice of reference wind speed leads to a shift in these data points towards lower wind speeds.

545 Sub-figures e and f show the wind speed probability distribution for the chosen average reference wind speeds between 100 and 300 m (bars), at 100 m WT hub-height (red line) and the standard Rayleigh distribution $U_{\text{ave}}^{\text{onshore}} = 10 \text{ ms}^{-1}$ and $U_{\text{ave}}^{\text{offshore}} = 12 \text{ ms}^{-1}$ International Electrotechnical Commission (2010). These distributions, together with the power curve are used to generate the annual energy distribution in sub-figures g and h. Especially onshore, AWES and WT

In contrast to conventional WT with their fixed hub-height, AWES adapt their operating heights dynamically, which makes the choice of reference wind speed non-trivial. Due to many conceptually different AWES designs and the novelty of the technology, there is no unanimously generally accepted AWES power curve definition exists. Similarly, no standard wind speed probability distribution resource model such as the Rayleigh or Weibull distribution for conventional wind has been defined. Figure 20 investigates the impact of different reference heights on AWES power curve representations (a,b) These power curves are derived from curve fits of 3 wind velocity profiles within each of the k=20 clusters. Offshore (orange) power curves are almost unaffected by the choice of reference height, as power curve almost collapse onto a single trend line. In contrast, onshore (blue) higher wind shear leads to spread out power curves. Together with differing wind speed probability distribution (c,d) this leads to varying annual energy distribution (e,f) and therefore AEP (sub-section 5.4). WT data with reference wind speed at $z = 100\text{m}$ (black dashed lines) and QSS data with an average reference wind speed between $100 \leq z \leq 300\text{m}$ (solid lines) are included for comparison. Clustered WRF profiles are compared to logarithmic wind speed profiles, as defined in the IEC standards. Therefore, no standard reference wind speed, equivalent to wind speed at hub height for conventional WT, has been agreed upon. Determining these parameters is more complex than for conventional wind turbines as AWES power is highly depends on the wind speed variation with height and the resulting flight trajectories.

The dashed lines are curves based on a fixed reference height of $z = 100\text{m}$. The dash-dotted lines use the average wind speed between $z = 100\text{m}$ and $z = 300\text{m}$ and the dotted lines use the average wind speed over the respective AWES operating altitude. AWES power curves for logarithmic wind speed profiles with $z_0 = 0.1$ (onshore, left) and $z_0 = 0.001$ (offshore, right) Burton (2011) as well as results using a simple WT power estimation (red) with a fixed $c_p^{\text{WT}} = 0.45$ (see equation: 9) are depicted as reference. The Hub height z_{WT} is assumed to be 100m for both onshore and offshore WT. The swept area of the turbine is chosen such that its rated power, at rated wind speed of $v_{\text{rated}} = 12\text{ms}^{-1}$, is equivalent to the AWES using:

$$P_{\text{WT}} = c_p^{\text{WT}} \frac{1}{2} \rho_{\text{air}} A_{\text{WT}} U^3 (z_{\text{WT}} = 100\text{m}) \quad (9)$$

Air density ρ_{air} is calculated as a function of altitude z from a linear approximation of the standard atmosphere ($\rho_{\text{air}}(z) = 1.225\text{kgm}^{-3}$ Champion et al..

Cut-in and cut-out wind speeds were not used for either the AWES or WT, to not limit specific designs. Therefore, energy production (bottom) is limited by the wind speed probability distribution (center). Wind statistics for the logarithmic wind speed profiles are based on the IEC standard Rayleigh distribution International Electrotechnical Commission (2010) with a reference wind speed of $U_{\text{ave}}^{\text{onshore}} = 10\text{ms}^{-1}$ and $U_{\text{ave}}^{\text{offshore}} = 12\text{ms}^{-1}$. The presented AWES and WT start producing significant power around $U \approx 5\text{ms}^{-1}$ and reach rated power between U 12 and 15ms^{-1} at their respective reference heights. Whereas the onshore AWES power curve with a fixed reference height of 100m almost aligns with the power curve of a conventional wind turbine, other power curves are seemingly below that. This is likely caused by higher wind shear profiles which lead to faster winds aloft and higher operating altitudes with lower wind speeds at 100m . The lower reference wind speeds, i.e. wind speeds at lower altitudes, result in a power curve shift towards lower wind speeds (to the left). Offshore winds however experience less shear (see sub-section : 2.2), which is why offshore AWES power curves for any reference height overlap with

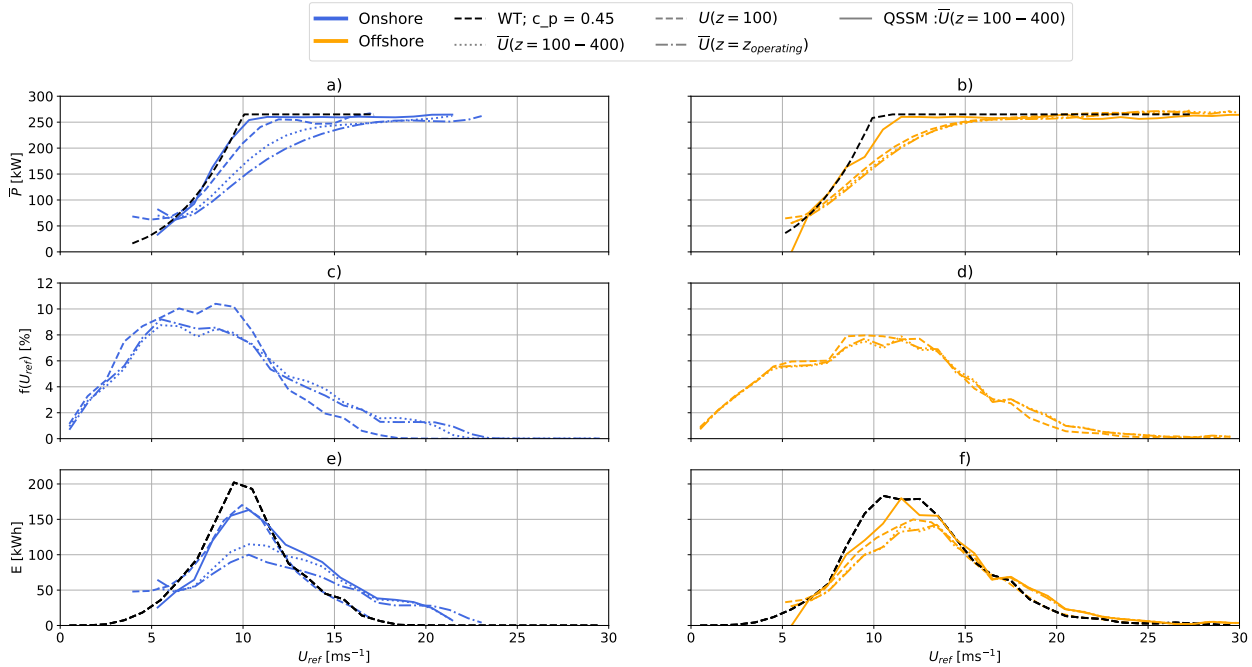


Figure 20. Onshore (blue) and offshore (orange) AWES power curves (a,b) over various reference wind speeds (dashed lines: fixed height $z = 100$ m; dotted lines: $z = 100 - 300$ m; dash-dotted lines: average wind speed along operating trajectory) based on 3 wind profiles for each of the $k=20$ clusters. A simplified WT (dashed black lines) and QSS AWES model (solid line) with same rated power are depicted as reference. Power curves and WRF-simulated annual wind speed probability distribution (c,d) for various reference heights result in annual energy production distribution (e,f) and AEP estimates.

580 each other. ~~Therefore, a reference height of 200 m is likely a better choice as it results in smoother power curve.~~ **Markus:**
~~move judgement to AEP section. this approach seems to OVERestimate AEP, cluster interpolation is generally lower~~
 see 22 The difference between onshore and offshore power curves is caused by different wind profile shapes because the design
 of both systems is the same. ~~This highlights that for AWES power predictions is not just influenced by design, but also by flight~~
~~trajectory in a given boundary layer. The AWES power curves align well with $c_p^{WT} = 0.3$ (see figure A5 in the appendix). A~~
 585 ~~better AWES design with higher c_L^3/c_D^2 should increase the equivalent WT power coefficient. This however is subject to further~~
~~investigation and will be included in a future study.~~

Multiplying power curve and wind speed probability distribution yields the annual energy production distribution E (e,f in
 figure 20. ~~is derived from the integral multiplication of the mean power curve (top) and the wind speed probability distribution~~
~~at reference height (center). Its total~~ The area underneath the distribution accumulates to the annual energy production (AEP)
 590 further analyzed in sub-section 5.4. AWES energy production distribution is shifted ~~shifts~~ towards higher wind speeds, particu-
 larly onshore, due to higher ~~operating heights~~ average wind speeds at operating height. Furthermore, the distribution of AWES

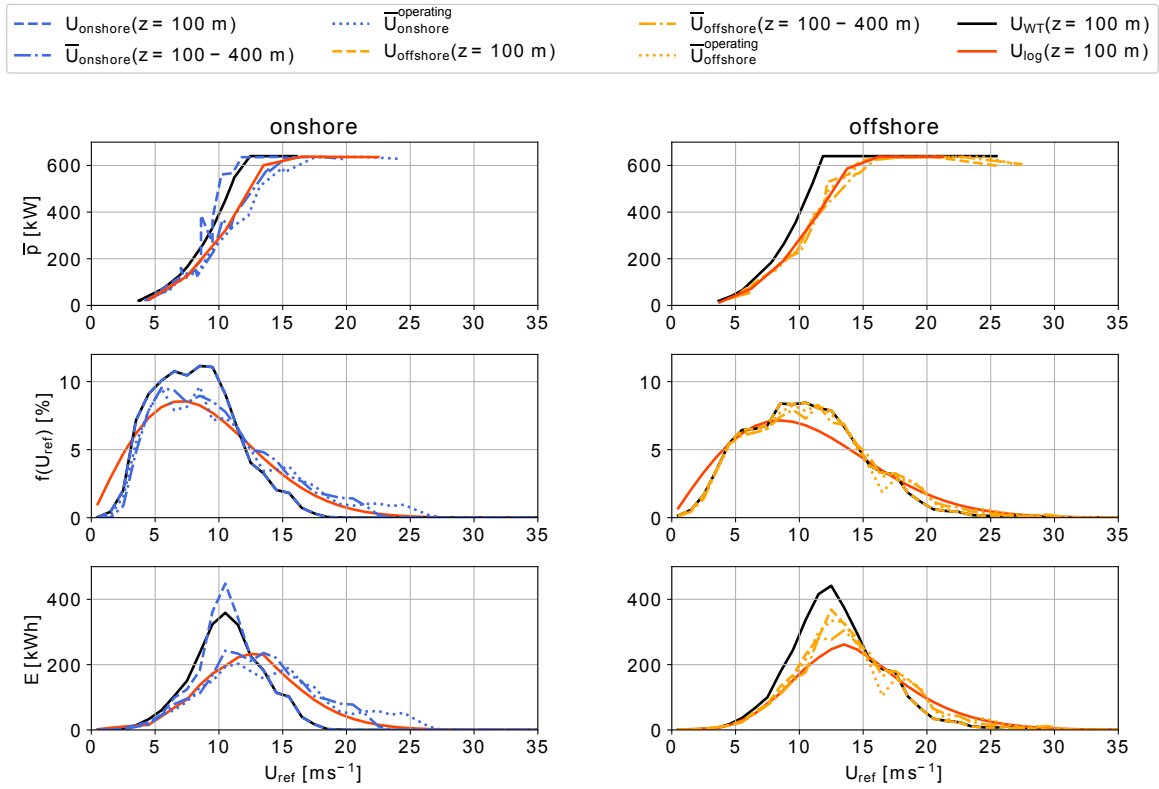


Figure 21. AWES power curves onshore (top left, blue) and offshore (top right, orange) for $A_{\text{wing}} = 20 \text{ m}^2$ over various reference wind speed height definitions (dashed-lines: fixed height $z = 100 \text{ m}$; dash-dotted-lines: fixed height range $z = 100 - 300 \text{ m}$; dotted-lines: average wind speed along operating trajectory) based on 3 profiles for each of the $k=20$ clusters. Compared to WT (black) with same rated power at a hub height of $z_{\text{WT}} = 100 \text{ m}$ and AWES (red) for logarithmic wind speed profiles ($z_0 = 0.1$ onshore and $z_0 = 0.001$ offshore). Annual wind speed probability distribution (center) based on WRF simulation and Rayleigh distribution (red) with $U_{\text{ave}} = 10 \text{ ms}^{-1}$ (onshore) and 12 ms^{-1} (offshore) for reference. Energy production distribution (bottom) shows the distribution of annual produced energy over wind speed which is the product of power and wind speed probability distribution. Integrating this product results in the AEP.

energy production shows a wider spread as the system operates within a wider range of wind speeds. Similarly, the maximum onshore wind speed at 100 m is lower than offshore, while wind speeds at other reference heights are similar to offshore.

595 Table 4 compiles the AEP of both system sizes and both locations. The table also includes the estimated WT AEP for reference. Overall energy estimates for one system size and location are fairly consistent with each other. However, energy estimates of the larger wing ($A_{\text{wing}} = 50 \text{ m}^2$) onshore shows more variability due to the wider range of wind conditions and operating heights. This indicates that this effect scales with system size increase which will be investigated further in a future study.

We assume that the best reference wind speed would be the wind speed along the actual AWES trajectory. Since this is hard to estimate before site selection, a better reference wind speed would be calculated from the average between 100 and 300 m since this is the height range at which most onshore and offshore AWES operate (see figure 18). Choosing one fixed reference height might be an inadequate choice as larger AWES sweep a larger altitude range.

Ref2: The fit for c_p is a function of c_{wing} (and because AR is constant, a function of A_{swept}) so it's not non-dimensional and it's not clear how generalizable it is (changes in AR or L/D). I'm curious about whether another definition of c_p may also be comparable to conventional wind turbines but work better. The Loyd paper (see eqs. 1 and 16) shows a limit on a c_p ($4/27 CL^3/CD^2$) defined by wing area. What does your data show for a c_p defined by A_{wing} ? Or if you express c_p as a function of L/D or CL^3/CD^2 ? Mark: My biggest concern about the AEP methodology is the mapping of the high dimensional space describing the wind profiles ($60*2=120$ dimensions?) to a 1D space (see figure 12). How would you justify integrating over only this 1D space? How accurate would this be? Do you also use p5, p50 and p95 wind profiles to the construct frequency distributions or only for the power curves? Markus: don't understand. I introduce and use average wind speed between 100 and 300 m as a proxy, using anything else would be too unreadable / incomprehensible

Table 4. Annual energy predictions (AEP) and capacity factor (cf) results for $A_{\text{wing}} = 20, 50 \text{ m}^2$ subject to 3 wind velocity profiles within each of the k=20 onshore and offshore clusters. AEP calculated from power curve and wind speed probability distributions at various reference heights (see figure 21 and A4). AEP results for logarithmic wind speed profiles with Rayleigh wind speed probability distribution and WTs (size in rotor diameter d_{WT}) with same rated power as AWESs and wind speed probability distribution at $z_{\text{WT}} = 100\text{m}$ for reference.

P_{rated} [kW]	size	location	wind profile	z_{ref} [m]	AEP [kWh]	cf [-]
650	$A_{\text{wing}} = 20\text{m}^2$	onshore	WRF	100	2329	0.42
	$A_{\text{wing}} = 20 \text{ m}^2$		WRF	100 - 400	2404	0.43
	$A_{\text{wing}} = 20 \text{ m}^2$		WRF	60 - 629	2324	0.42
	$A_{\text{wing}} = 20 \text{ m}^2$		log	100	2216	0.40
	$d_{\text{WT}} = 42.6 \text{ m}$		WRF	100	2292	0.41
650	$A_{\text{wing}} = 20 \text{ m}^2$	offshore	WRF	100	2853	0.51
	$A_{\text{wing}} = 20 \text{ m}^2$		WRF	100 - 400	2852	0.51
	$A_{\text{wing}} = 20 \text{ m}^2$		WRF	59 - 551	2910	0.52
	$A_{\text{wing}} = 20 \text{ m}^2$		log	100	2781	0.50
	$d_{\text{WT}} = 42.6 \text{ m}$		WRF	100	3404	0.61
2600	$A_{\text{wing}} = 50 \text{ m}^2$	onshore	WRF	100	7863	0.34
	$A_{\text{wing}} = 50 \text{ m}^2$		WRF	100 - 400	8069	0.35
	$A_{\text{wing}} = 50 \text{ m}^2$		WRF	75 - 702	7529	0.32
	$A_{\text{wing}} = 50 \text{ m}^2$		log	100	7252	0.31
	$d_{\text{WT}} = 83.4 \text{ m}$		WRF	100	8961	0.39
2600	$A_{\text{wing}} = 50 \text{ m}^2$	offshore	WRF	100	9381	0.41
	$A_{\text{wing}} = 50 \text{ m}^2$		WRF	100 - 400	9349	0.41
	$A_{\text{wing}} = 50 \text{ m}^2$		WRF	75 - 1265	9540	0.41
	$A_{\text{wing}} = 50 \text{ m}^2$		log	100	9542	0.41
	$d_{\text{WT}} = 83.4 \text{ m}$		WRF	100	13518	0.59

5.4 AEP

615 This sub-section contrasts annual energy predictions (AEPs) and capacity factor (cf) based on the various power estimates and
 wind statistics. Figure 23 compares results for an increasing number of clusters $k=2,5,10,20,30,40,50,100$ to results using
 p5, p50, p95 wind velocity profiles for $k=20$ to assess the necessary number of clusters and therefore optimization runs needed
 to approximate the simulated AWES AEP. The top sub-figure shows results for an AWES wing of $A_{\text{wing}}=20 \text{ m}^2$ and bottom
 620 for $A_{\text{wing}}=50 \text{ m}^2$. Onshore results are depicted in blue and offshore data in orange. Power results of the k cluster sweep
 are solely based on each cluster's centroid which is equivalent to the average wind velocity profiles of all data points within
 the respective cluster. Here we assume that the power calculated from each centroid is constant within and representative of
 the entire cluster. Therefore, AEP is the sum of the product of average power \bar{P}_i and cluster probability f_i over all clusters k
 multiplied by the number of hours in a year. Conventional WT energy (dashed line) is estimated from a simple static power
 approximations (described in sub-section 5.3, equation 9) using cluster centroid wind speed at 100 m and the same cluster
 frequency as the AWES.

$$625 \quad \underline{AEP} = \sum_{i=1}^k (\bar{P}_i f_i) 8760 \frac{\text{h}}{\text{year}} \quad (10)$$

Figure 23 shows AEP predictions based on power predictions for p5, p50, p95 wind velocity profiles of $k = 5, 10, 20, 50$
 clusters for 3 reference heights ($\text{AWES}(z = 100\text{m})$, $\text{AWES}(100\text{m} \leq z \leq 300\text{m})$, $\text{AWES}(z_{\text{oper}})$). These data are compared to
 QSS and WT reference models as well as optimized AWES performance estimated based on logarithmic wind speed profiles
 ($\text{AWES}_{\text{log}}(z = 100)$) and a Rayleigh distribution at 100 m. Additionally, AEP is assessed from a power summation over every
 630 10-min wind speed profile within each cluster ($\text{AWES}_{\text{cluster}}$).

Both onshore (blue) and offshore (orange) AEP vary with number of clusters, however above $k=10$ 20 the variation is
 negligible and the possible improvement in energy prediction does not justify the increased computational cost. Less wind shear
offshore results in decreased spread between reference heights. AEP predictions of $\text{AWES}_{\text{cluster}}$ are generally lower than other
estimates and closest to $\text{AWES}(z_{\text{operating}})$, which could indicate that these are more realistic estimates. At both locations, the
 635 QSS model seems to over predict AEP, due to the simplifying assumptions. Onshore, AEP is particularly high, because of the
higher wind speeds at between $100\text{m} \leq z \leq 300\text{m}$. The simplified WT model seemingly outperforms the dynamic optimization
AWES model, particularly offshore where lower wind shear only slightly increases energy yield at higher altitudes. Logarithmic
wind speed profiles 4.7 and Rayleigh wind speed probability distributions ($U_{\text{ave}}^{\text{onshore}} = 10 \text{ ms}^{-1}$ and $U_{\text{ave}}^{\text{offshore}} = 12 \text{ ms}^{-1}$) also
predict higher AEP than WRF-simulated wind conditions. Offshore AEP estimates based on logarithmic wind profiles are
 640 closer to power curve estimates based on WRF data than similar onshore results. This implies that offshore wind conditions
(wind profile shape and probability) are better represented by logarithmic wind speed profiles than onshore conditions.

Similarly, WT AEP does not vary significantly for more than 10 clusters. However, AEP and cf are consistently higher than
 those of AWES. Compared to these results, AEP calculations based on an estimated power curve from three representative
 wind profiles per cluster $k=20$ (◆ see sub-section 5.3 ; color refers to location, onshore: blue, offshore: orange) yield a higher

645 energy estimate. Estimates using just the centroid have lower AEP because of averaging effects within each cluster. High wind speed profiles, which are responsible for a considerable percentage of the cluster energy due to the nonlinear power to wind speed relationship, are averaged out. We therefore believe that a power curve estimation together with wind speed probability distribution for a lower number of total clusters and multiple profiles within a cluster yield better AEP estimates than just using the cluster centroids.

650 Reference AWES AEP and ef are depicted as dotted lines. These data are based on power curves for logarithmic wind speed profiles (with $z_0 = 0.1$ onshore and $z_0 = 0.001$ offshore) and Rayleigh wind speed probability distributions ($U_{ave}^{onshore} = 10 \text{ ms}^{-1}$ and $U_{ave}^{offshore} = 12 \text{ ms}^{-1}$). Offshore AEP estimates based on logarithmic wind profiles are closer to power curve estimates based on WRF data than similar onshore results. This implies that offshore wind conditions (wind profile shape and probability) are better represented by logarithmic wind speed profiles than onshore conditions. Mark: high k close to running every profile, therefore best. The trends in figure 14 don't converge to the diamond-marked value (k=20,p5,p50,p95-profiles) for very large k. This suggests that eccentric wind profiles are over-represented in the AEP calculation using the p5,p50,p95-profiles. Markus: not sure if the eccentric profiles are over represented. This data is based on interpolated power curves and using just the cluster centroids averages out the high wind speeds

655 Mark: Legends are confusing: different entries for line colors and styles and some combinations are missing (e.g. no round blue marker is included, while a square blue marker is and there is no separate general entry for a solid line). It would be good to be a bit more consistent.

660

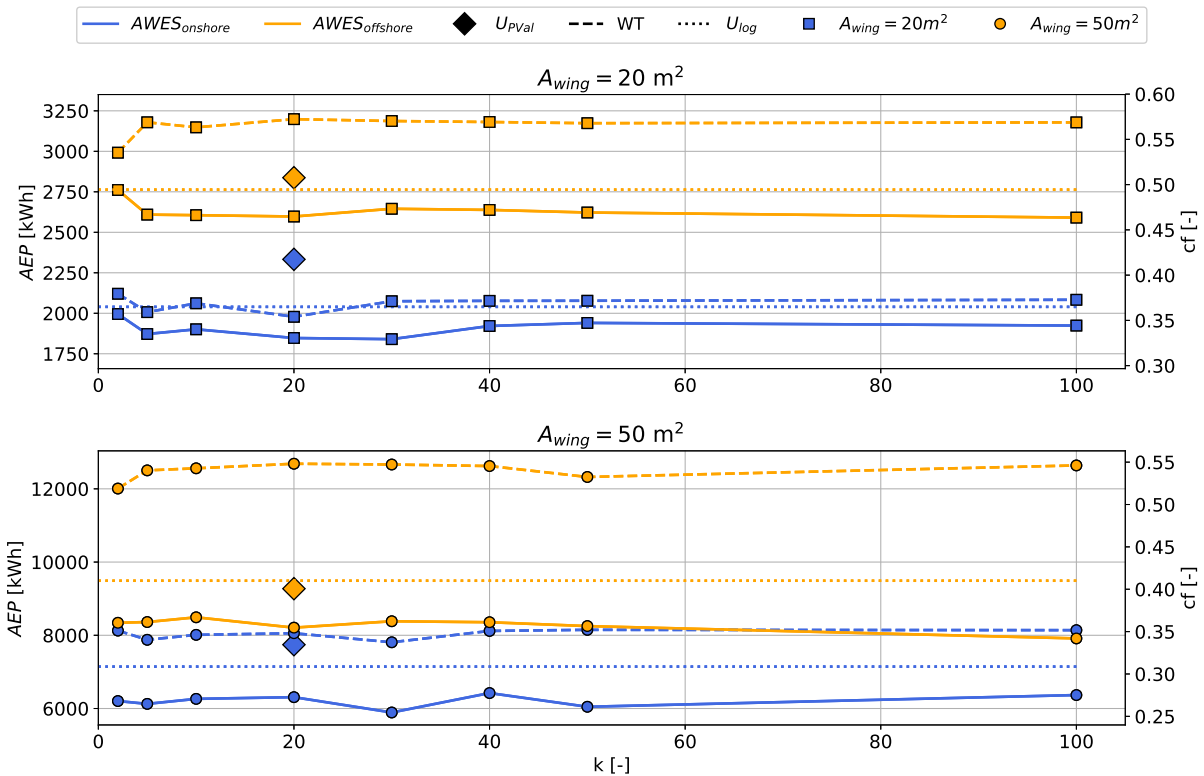


Figure 22. AEP (left ordinate) and cf (right ordinate) over number of clusters k for AWES with a wing area of $A_{wing} = 20 \text{ m}^2$ (top) and $A_{wing} = 50 \text{ m}^2$ (bottom) onshore (blue) and offshore (orange) location. Only the cluster centroid wind velocity profiles and the cluster probability were used for both AWES (solid lines) and WT (dashed lines). The WT power is estimated from a static power curve ($z_{WT} = 100 \text{ m}$, see equation 9). AWES results are derived from trajectory optimization using the `awebox` (see section 4). AWES data for p5, p50, p95 wind profiles within $k=20$ clusters (\blacklozenge ; applies to both locations and sizes) are calculated from the mean power curve and wind speed probability (see table 4, sub-section 5.3). AWES results based on logarithmic wind speed profiles (dotted lines) are added for reference.

6 Conclusions and outlook

Mark: miss critical discussion about what data is suited for your methodology. Why need WRF and not re-analysis data? re-analysis more trustworthy because data assimilation?

665 using fewer profiles gives best AEP, doesn't that mean that you discard most of WRF data anyways?

would even expect that the data of a coarser model would be better suited for this context, as especially the p5 and p95 profiles are less prone to being eccentric, outlying wind profiles and thereby more representative.

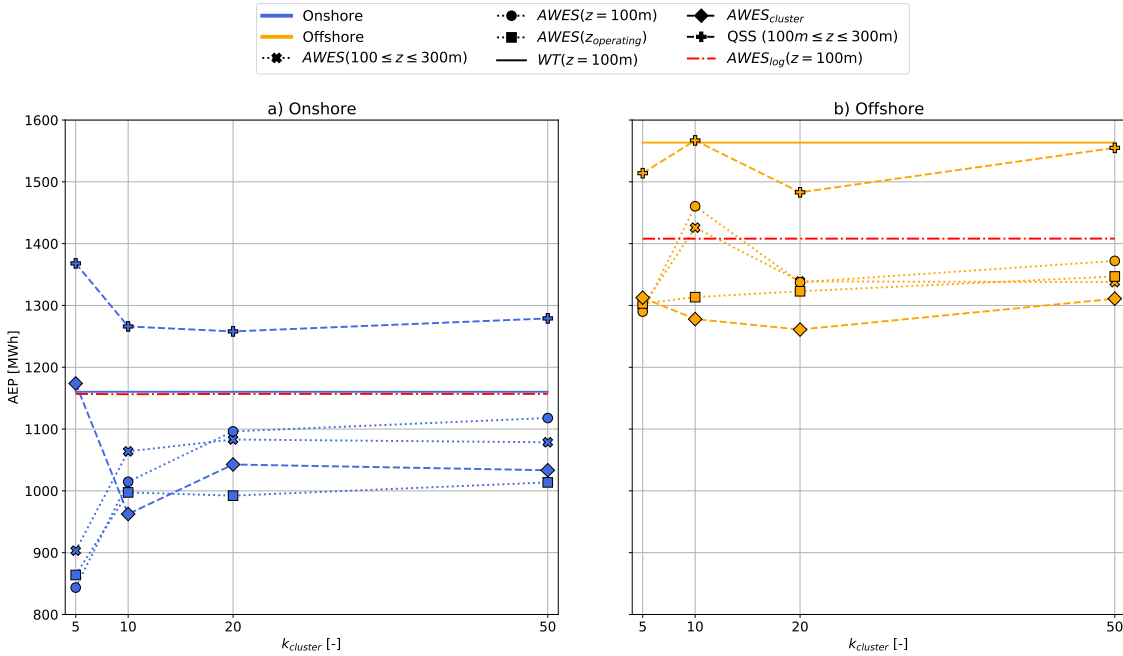


Figure 23. Onshore (a) and offshore (b) AEP over number of clusters k based on power curve and wind speed distribution in sub-section 5.3 over various reference heights. QSS (+) and WT (solid lines) reference models as well as optimized AWES performance estimated based on logarithmic wind speed profiles (red dash dotted lines) and a Rayleigh distribution at 100 m. $AWES_{cluster}$ estimates AWES AEP based on the summation of interpolated power within each cluster.

We characterized evaluated ground-generation AWES power, annual energy production and capacity factor, operating heights and tether lengths based on representative, mesoscale onshore wind data at Pritzwalk in northern Germany and offshore wind data at the FINO3 research platform in the North Sea. The analysis is deduced from uses the awebox toolbox to generate power-optimized AWES trajectories path-optimization using awebox toolbox, with the objective to maximize average cycle power. Representative wind velocity profiles based on k-means clustering were chosen to reduce computational cost. As long-term high resolution high altitude measurements with sufficient data availability are scarce, wind data are based on mesoscale WRF simulations. These simulations span an entire year with a temporal resolution of 10 minutes, thereby including seasonal, synoptic and diurnal variations at a higher resolution than re-analysis data sets. The annual wind roses for heights of 100 m and 500 m confirm the expected wind speed acceleration increase and clockwise rotation at both locations, with generally lower offshore wind shear and veer than onshore. Annual wind speed statistics reveal that while average wind speeds increase with height, low wind speeds still occur at a fairly high probability up to 1000 m.

To further dissect wind conditions essential to the design and operation of AWES and to reduce computational cost, representative wind velocity profiles were chosen based on k-means clustered data. This algorithm groups similar profiles together into a fixed, predetermined number of k clusters represented by the mean of each cluster. For a representative k of 10 (chosen

for visualization purposes) a more extensive analysis and comparison between onshore and offshore wind conditions revealed that average wind speed, rather than profile shape, plays a decisive role in the assignment of assigning profiles to a certain cluster. However, the algorithm was able to identify and define a cluster for onshore LLJs as well as various non-logarithmic wind profiles at both locations. Further analysis revealed seasonal and diurnal wind speed and atmospheric stability dependent cluster correlation, which generally agrees with literature predictions. We therefore believe that k-means wind velocity clustering yields coherent data that provides good insight into the wind regime, especially for higher altitudes. The derived groups represent the annual variation better than traditional conventional logarithmic or exponential wind speed profiles.

Three representative wind velocity profiles based on the 5th, 50th and 95th percentile wind velocity profiles within each cluster for $k=20$ as well as logarithmic reference wind speed profiles were implemented used as input into the airborne wind energy trajectory optimization toolbox `awebbox` to estimate average cycle power of ground-generation AWES. Two A scaled Ampyx AP2 aircraft sizes ($A_{wing} = 20 \text{ m}^2$) are compared is analyzed in terms of trajectory, operating altitude, instantaneous tether force and length as well as power and AEP. AWESs at both location rarely operate above 300 m, with offshore systems mostly flying below 200 m, due to fast high wind speeds at lower heights and low wind shear. These results weaken the claim of increased power harvest above 500 m for AWES, but also obviate airspace restriction challenges for AWES. Simplified quasi-steady state (QSS) AWES as well as WT models are used to contextualize the optimization results. The WT model reaches rated power at lower wind speeds, because tether losses decrease AWES power, which the QSS AWES model can not fully capture. A wing with the given size, aerodynamic and mass properties achieves a similar power curve as a similarly rated wind turbine with a power coefficient of approximately 0.3. As expected, offshore AWES generally outperform onshore AWES in terms of AEP and capacity factor. Furthermore, social acceptance of such systems will likely be higher offshore.

Beneficial offshore wind conditions lead to higher AWES AEP than onshore. However, relative to the WT reference model, which generally predicts higher AEP, onshore AWES perform slightly better due to higher wind shear and higher wind speeds aloft. AEP estimates of the QSS AWES model are higher than dynamic results, because it does not capture power variation along the flight path and under predicts tether losses. Probably the most realistic, but also lowest energy yield predictions are derived from wind speed distribution at operating height $AWES_{operating}$ and the sum of interpolated power within each cluster $AWES_{cluster}$. AWES AEP based on logarithmic wind profiles and Rayleigh wind speed distributions predict higher yield than AEP based on clustered WRF-simulated wind resource, indicating that the conventional approach can not reproduce the impact of realistic wind conditions on AWES performance. Comparing WRF-clustered AEP for different power and wind resource descriptions show that the benefit of using more than $k=20$ clusters are marginal. Using the wind speed distribution at a fixed reference height of 100 m leads to an over prediction of annual energy, particularly onshore. A better reference could be average wind speed between 100 - 300 m because AWES mostly operate within this range and AEP estimates are closer to AEP of $AWES_{operating}$ and $AWES_{cluster}$. However, the choice of reference height for the derivation of the wind speed probability distribution is more important onshore, due to higher wind shear and more non-monotonic wind speed profiles.

From this analysis we derived an AWES power coefficient c_p^{AWES} based on average AWES power curves, path lengths and wing spans. The decrease in c_p^{AWES} with wind speed can be attributed to the increase in tether length and the accompanying

~~weight and drag losses. Sealing these power coefficients by the inverse wing chord (c_p^{AWES}/c_{wing}) lead to a collapse of both location and both size trends to a single quadratic, decreasing progression.~~

720 ~~We compare AEP and cf estimates for each system based on different power and wind speed probability description and conclude that the highest, and probably most realistic AEP prediction, is based on an average power curve which is derived from multiple wind profiles within a cluster (p5, p50, p95) for a small number of clusters (k=10). The wind speed probability distribution is ideally derived from the wind speed along the flight path. As this is difficult to predetermined before operation, we recommend to use average wind speeds between 100 and 400 m. Offshore this choice seems to be less significant as winds are less sheared and are more monotonic than onshore. Therefore, AEP estimates based on logarithmic wind profiles and Rayleigh distribution give similar results as the clustered profiles.~~

725 In summary, k-means clustering provides adequate categorization and **provides** realistic, representative wind velocity profiles for AWES trajectory optimization. Thereby, increasing the accuracy of AWES power prediction in comparison to logarithmic wind speed profiles. Furthermore, clustering reduces the computational cost of power curve and AEP estimates as **only a few**
730 **a low** number of clusters suffices. **Best Good** AEP results and power curve description can be achieved by using multiple representative profiles within each cluster. ~~instead of using the cluster centroid. A nonlinear AWES power coefficient to approximate AWES power up to rated power gives reasonable results. We expect further work, field tests and other research studies with different AWES sizes, aerodynamic coefficients and flight paths to confirm our findings.~~

Based on these results, we will describe the design space and weight budget of ground-generation AWES in a future sizing study using the here described clustered wind data. To that end, we will compare the performance of a high lift airfoil to the here used AP2 aerodynamic reference model and determine the maximum weight for different aircraft sizes. ~~Furthermore, we~~
735 ~~will investigate the impact of a nonlinear lift coefficient. These results should inform researchers and industry on the sealing potential of AWES. An investigation of measured power curves and real AEP is necessary to confirm or disproof the models used in this paper. The description of the AWES wind resource, particularly onshore, needs further analysis as is highly affects AWES energy yield predictions.~~ An interesting research question is the seasonality of AWES performance in comparison to WT.

740 **6.1 Acknowledgments and funding sources**

The authors thank the BMWi for funding of the “OnKites I” and “OnKites II” project [grant number 0325394A] on the basis of a decision by the German Bundestag and project management Projektträger Jülich. We thank the PICS, NSERC and the DAAD for their funding.

745 `awebox` has been developed in collaboration with the company Kiteswarms Ltd. The company has also supported the `awebox` project through research funding. The `awebox` project has received funding from the European Union’s Horizon 2020 research and innovation program under the Marie Skłodowska-Curie grant agreement No 642682 (AWESCO)

We thank the Carl von Ossietzky University of Oldenburg and the Energy Meteorology research group for providing access to their **H**high **P**performance **C**computing cluster *EDDY* and ongoing support.

We further acknowledge Rachel Leuthold (University of Freiburg, SYSCOP) and Thilo Bronnenmeyer (Kiteswarms Ltd.)
750 for their helped in writing this article, great, technical support and continued work on the awebox.

6.2 Author contribution

Markus Sommerfeld evaluated the data and wrote the manuscript in consultation and under the supervision of Curran Crawford.
Martin Dörenkämper set up the numerical offshore simulation, contributed to the meteorological evaluation of the data and
755 reviewed the manuscript. Jochem De Schutter co-developed the optimization model and helped writing and reviewed this
manuscript.

References

- Ampyx: Ampyx Power BV, <https://www.ampyxpower.com/>, last accessed: 30.10.2020, 2020.
- Andersson, J. A. E., Gillis, J., Horn, G., Rawlings, J. B., and Diehl, M.: CasADi – A software framework for nonlinear optimization and optimal control, *Mathematical Programming Computation*, 11, 1–36, <https://doi.org/10.1007/s12532-018-0139-4>, 2019.
- 760 Archer, C. L., Colle, B. A., Veron, D. L., Veron, F., and Sienkiewicz, M. J.: On the predominance of unstable atmospheric conditions in the marine boundary layer offshore of the U.S. northeastern coast, *Journal of Geophysical Research: Atmospheres*, 121, 8869–8885, <https://doi.org/10.1002/2016JD024896>, <https://agupubs.onlinelibrary.wiley.com/doi/abs/10.1002/2016JD024896>, 2016.
- Argatov, I. and Silvennoinen, R.: Efficiency of Traction Power Conversion Based on Crosswind Motion, pp. 65–79, Springer Berlin Heidelberg, Berlin, Heidelberg, https://doi.org/10.1007/978-3-642-39965-7_4, https://doi.org/10.1007/978-3-642-39965-7_4, 2013.
- 765 Arya, P. and Holton, J.: Introduction to Micrometeorology, International Geophysics, Elsevier Science, 2001.
- Aull, M., Stough, A., and Cohen, K.: Design Optimization and Sizing for Fly-Gen Airborne Wind Energy Systems, *Automation*, 1, 1–16, 2020.
- Banta, R. M.: Stable-boundary-layer regimes from the perspective of the low-level jet, *Acta Geophysica*, 56, 58–87, <https://doi.org/10.2478/s11600-007-0049-8>, <https://doi.org/10.2478/s11600-007-0049-8>, 2008.
- 770 Bronnenmeyer, T.: Optimal Control for Multi-Kite Emergency Trajectories, Master’s thesis, University of Stuttgart, <https://cdn.syscop.de/publications/Bronnenmeyer2018.pdf>, 2018.
- Burton, T., ed.: Wind energy handbook, Wiley, Chichester, West Sussex, 2nd ed edn., <https://doi.org/10.1002/9781119992714>, 2011.
- Champion, K. S. W., Cole, A. E., and Kantor, A. J.: Chapter 14 Standard and Reference Atmospheres.
- Cherubini, A., Papini, A., Vertechy, R., and Fontana, M.: Airborne Wind Energy Systems: A review of the technologies, *Renewable and Sustainable Energy Reviews*, 51, 1461–1476, <https://doi.org/10.1016/j.rser.2015.07.053>, <http://linkinghub.elsevier.com/retrieve/pii/S1364032115007005>, 2015.
- 775 de Amorim, R. C. and Hennig, C.: Recovering the number of clusters in data sets with noise features using feature rescaling factors, *Information Sciences*, 324, 126–145, <https://doi.org/10.1016/j.ins.2015.06.039>, 2015.
- De Schutter, J., Leuthold, R., and Diehl, M.: Optimal Control of a Rigid-Wing Rotary Kite System for Airborne Wind Energy, in: Proceedings of the European Control Conference (ECC), 2018.
- 780 De Schutter, J., Leuthold, R., Bronnenmeyer, T., Paelinck, R., and Diehl, M.: Optimal control of stacked multi-kite systems for utility-scale airborne wind energy, in: 2019 IEEE 58th Conference on Decision and Control (CDC), pp. 4865–4870, 2019.
- Dee, D. P., Uppala, S. M., Simmons, A. J., Berrisford, P., Poli, P., Kobayashi, S., Andrae, U., Balmaseda, M. A., Balsamo, G., Bauer, P., Bechtold, P., Beljaars, A. C. M., van de Berg, L., Bidlot, J., Bormann, N., Delsol, C., Dragani, R., Fuentes, M., Geer, A. J., Haimberger, L., Healy, S. B., Hersbach, H., Hólm, E. V., Isaksen, I., Kållberg, P., Köhler, M., Matricardi, M., McNally, A. P., Monge-Sanz, B. M., Morcrette, J.-J., Park, B.-K., Peubey, C., de Rosnay, P., Tavolato, C., Thépaut, J.-N., and Vitart, F.: The ERA-Interim reanalysis: configuration and performance of the data assimilation system, *Quarterly Journal of the Royal Meteorological Society*, 137, 553–597, <https://doi.org/10.1002/qj.828>, 2011.
- 785 Diehl, M.: Airborne Wind Energy: Basic Concepts and Physical Foundations, in: Airborne Wind Energy, edited by Ahrens, U., Diehl, M., and Schmehl, R., pp. 3–22, Springer Berlin Heidelberg, Berlin, Heidelberg, https://doi.org/10.1007/978-3-642-39965-7_1, https://doi.org/10.1007/978-3-642-39965-7_1, 2013.

- Donlon, C. J., Martin, M., Stark, J., Roberts-Jones, J., Fiedler, E., and Wimmer, W.: The Operational Sea Surface Temperature and Sea Ice Analysis (OSTIA) system, *Remote Sensing of Environment*, 116, 140–158, <https://doi.org/10.1016/j.rse.2010.10.017>, 2012.
- 795 Dörenkämper, M., Optis, M., Monahan, A., and Steinfeld, G.: On the Offshore advection of Boundary-Layer Structures and the Influence on Offshore Wind Conditions, *Boundary-Layer Meteorol.*, 155, 459–482, <https://doi.org/10.1007/s10546-015-0008-x>, 2015.
- Dörenkämper, M., Stoevesandt, B., and Heinemann, D.: Derivation of an offshore wind index for the German bight from high-resolution mesoscale simulation data, *Proceedings of DEWEK - German Offshore Wind Energy Conference*, p. 5, 2017.
- Dörenkämper, M., Olsen, B. T., Witha, B., Hahmann, A. N., Davis, N. N., Barcons, J., Ezber, Y., García-Bustamante, E., González-Rouco, J. F., Navarro, J., Sastre-Marugán, M., Sile, T., Trei, W., Žagar, M., Badger, J., Gottschall, J., Sanz Rodrigo, J., and Mann, J.: The 800 Making of the New European Wind Atlas – Part 2: Production and evaluation, *Geoscientific Model Development*, 13, 5079–5102, <https://doi.org/10.5194/gmd-13-5079-2020>, <https://gmd.copernicus.org/articles/13/5079/2020/>, 2020.
- Echeverri, P., Fricke, T., Homsy, G., and Tucker, N.: The Energy Kite - Selected Results From the Design, Development and Testing of Makani's Airborne Wind Turbines - Part 1, Technical Report 1, Makani Power, https://storage.googleapis.com/x-prod.appspot.com/files/Makani_TheEnergyKiteReport_Part1.pdf, 2020.
- 805 Eijkelhof, D., Rapp, S., Fasel, U., Gaunaa, M., and Schmehl, R.: Reference Design and Simulation Framework of a Multi-Megawatt Airborne Wind Energy System, *Journal of Physics: Conference Series*, 1618, 032 020, <https://doi.org/10.1088/1742-6596/1618/3/032020>, <https://doi.org/10.1088/1742-6596/1618/3/032020>, 2020.
- Emeis, S.: *Wind energy meteorology: atmospheric physics for wind power generation*, Springer, Heidelberg, 2018.
- Fagiano, L. and Milanese, M.: Airborne Wind Energy: An overview, in: 2012 American Control Conference (ACC), pp. 3132–3143, 810 <https://doi.org/10.1109/ACC.2012.6314801>, 2012.
- Floors, R., Batchvarova, E., Gryning, S.-E., Hahmann, A. N., Peña, A., and Mikkelsen, T.: Atmospheric boundary layer wind profile at a flat coastal site - wind speed lidar measurements and mesoscale modeling results, *Advances in Science and Research*, 6, 155–159, <https://doi.org/10.5194/asr-6-155-2011>, <http://www.adv-sci-res.net/6/155/2011/>, 2011.
- Gaertner, E., Rinker, J., Sethuraman, L., Zahle, F., Anderson, B., Barter, G. E., Abbas, N. J., Meng, F., Bortolotti, P., Skrzypinski, W., 815 Scott, G. N., Feil, R., Bredmose, H., Dykes, K., Shields, M., Allen, C., and Viselli, A.: IEA Wind TCP Task 37: Definition of the IEA 15-Megawatt Offshore Reference Wind Turbine, OSTI.gov, <https://doi.org/10.2172/1603478>, 2020.
- Gros, S., Zanon, M., and Diehl, M.: A relaxation strategy for the optimization of airborne wind energy systems, in: *Control Conference (ECC)*, 2013 European, pp. 1011–1016, IEEE, http://ieeexplore.ieee.org/xpls/abs_all.jsp?arnumber=6669670, 2013.
- Haas, T., Schutter, J. D., Diehl, M., and Meyers, J.: Wake characteristics of pumping mode airborne wind energy systems, *Journal of Physics: 820 Conference Series*, 1256, 012 016, <https://doi.org/10.1088/1742-6596/1256/1/012016>, <https://doi.org/10.1088%2F1742-6596%2F1256%2F1%2F012016>, 2019.
- Hahmann, A. N., Sile, T., Witha, B., Davis, N. N., Dörenkämper, M., Ezber, Y., García-Bustamante, E., González-Rouco, J. F., Navarro, J., Olsen, B. T., and Söderberg, S.: The making of the New European Wind Atlas – Part 1: Model sensitivity, *Geoscientific Model Development*, 13, 5053–5078, <https://doi.org/10.5194/gmd-13-5053-2020>, <https://gmd.copernicus.org/articles/13/5053/2020/>, 2020.
- 825 Hersbach, H. and Dick, D.: ERA5 reanalysis is in production, <http://www.ecmwf.int/en/newsletter/147/news/era5-reanalysis-production>, last accessed: 22.10.2019, 2016.
- Houska, B. and Diehl, M.: Optimal control for power generating kites, in: 2007 European Control Conference (ECC), pp. 3560–3567, <https://doi.org/10.23919/ECC.2007.7068861>, 2007.
- HSL: The HSL Mathematical Software Library @ONLINE, <http://www.hsl.rl.ac.uk/>, 2020.

- 830 International Electrotechnical Commission, ed.: Design requirements: amendment 1, no. 1,1 in Wind turbines, IEC, Geneva, ed. 3.0, 2010-10 edn., oCLC: 838280539, 2010.
- Kaufman, L. and Rousseeuw, P. J.: Finding Groups in Data: An Introduction to Cluster Analysis, John Wiley, <https://doi.org/10.1002/9780470316801>, 1990.
- Kruijff, M. and Ruiterkamp, R.: A Roadmap Towards Airborne Wind Energy in the Utility Sector, pp. 643–662, Springer Singapore, Singapore, https://doi.org/10.1007/978-981-10-1947-0_26, https://doi.org/10.1007/978-981-10-1947-0_26, 2018.
- 835 Leuthold, R., De Schutter, J., Malz, E. C., Licitra, G., Gros, S., and Diehl, M.: Operational Regions of a Multi-Kite AWE System, in: 2018 European Control Conference (ECC), pp. 52–57, <https://doi.org/10.23919/ECC.2018.8550199>, 2018.
- Leuthold, R., De Schutter, J., Malz, E., Licitra, G., Bronnenmeyer, T., Gros, S., and Diehl, M.: *awebox*: Modelling and optimal control of single- and multiple-kite systems for airborne wind energy, <https://github.com/awebox>, 2020.
- 840 Licitra, G., Koenemann, J., Bürger, A., Williams, P., Ruiterkamp, R., and Diehl, M.: Performance assessment of a rigid wing Airborne Wind Energy pumping system, *Energy*, 173, 569–585, <https://doi.org/10.1016/j.energy.2019.02.064>, 2019.
- Loyd, M. L.: Crosswind kite power (for large-scale wind power production), *Journal of energy*, 4, 106–111, <http://arc.aiaa.org/doi/abs/10.2514/3.48021>, 1980.
- Lunney, E., Ban, M., Duic, N., and Foley, A.: A state-of-the-art review and feasibility analysis of high altitude wind power in Northern Ireland, *Renewable and Sustainable Energy Reviews*, 68, 899 – 911, <https://doi.org/https://doi.org/10.1016/j.rser.2016.08.014>, <http://www.sciencedirect.com/science/article/pii/S1364032116304282>, 2017.
- 845 Malz, E., Koenemann, J., Sieberling, S., and Gros, S.: A reference model for airborne wind energy systems for optimization and control, *Renewable Energy*, 140, 1004 – 1011, <https://doi.org/https://doi.org/10.1016/j.renene.2019.03.111>, <http://www.sciencedirect.com/science/article/pii/S0960148119304239>, 2019.
- 850 Malz, E., Hedenus, F., Göransson, L., Verendel, V., and Gros, S.: Drag-mode airborne wind energy vs. wind turbines: An analysis of power production, variability and geography, *Energy*, 193, 116 765, <https://doi.org/https://doi.org/10.1016/j.energy.2019.116765>, <http://www.sciencedirect.com/science/article/pii/S0360544219324600>, 2020.
- Molina-García, A., Fernández-Guillamón, A., Gómez-Lázaro, E., Honrubia-Escribano, A., and Bueso, M. C.: Vertical Wind Profile Characterization and Identification of Patterns Based on a Shape Clustering Algorithm, *IEEE Access*, 7, 30 890–30 904, <https://doi.org/10.1109/ACCESS.2019.2902242>, 2019.
- 855 Nakanishi, M. and Niino, H.: Development of an Improved Turbulence Closure Model for the Atmospheric Boundary Layer, *Journal of the Meteorological Society of Japan*, 87, 895–912, <https://doi.org/10.2151/jmsj.87.895>, 2009.
- Obukhov, A. M.: Turbulence in an atmosphere with a non-uniform temperature, *Boundary-Layer Meteorology*, 2, 7–29, <https://doi.org/10.1007/BF00718085>, 1971.
- 860 Olauson, J.: ERA5: The new champion of wind power modelling?, *Renewable Energy*, 126, 322–331, <https://doi.org/10.1016/j.renene.2018.03.056>, 2018.
- Optis, M., Monahan, A., and Bosveld, F. C.: Limitations and breakdown of Monin–Obukhov similarity theory for wind profile extrapolation under stable stratification, *Wind Energy*, 19, 1053–1072, <https://doi.org/10.1002/we.1883>, 2016.
- Peña, A., Gryning, S.-E., and Floors, R.: Lidar observations of marine boundary-layer winds and heights: a preliminary study, *Meteorologische Zeitschrift*, 24, 581–589, <https://doi.org/10.1127/metz/2015/0636>, http://www.schweizerbart.de/papers/metz/detail/24/84892/Lidar_observations_of_marine_boundary_layer_winds_?af=crossref, 2015.
- 865

- Pedregosa, F., Varoquaux, G., Gramfort, A., Michel, V., Thirion, B., Grisel, O., Blondel, M., Prettenhofer, P., Weiss, R., Dubourg, V., Vanderplas, J., Passos, A., Cournapeau, D., Brucher, M., Perrot, M., and Duchesnay, E.: Scikit-learn: Machine Learning in Python, *Journal of Machine Learning Research*, 12, 2825–2830, 2011.
- 870 Salvação, N. and Guedes Soares, C.: Wind resource assessment offshore the Atlantic Iberian coast with the WRF model, *Energy*, 145, 276 – 287, <https://doi.org/https://doi.org/10.1016/j.energy.2017.12.101>, <http://www.sciencedirect.com/science/article/pii/S0360544217321448>, 2018.
- Schelbergen, M., Kalverla, P. C., Schmehl, R., and Watson, S. J.: Clustering wind profile shapes to estimate airborne wind energy production, *Wind Energy Science*, 5, 1097–1120, <https://doi.org/10.5194/wes-5-1097-2020>, <https://wes.copernicus.org/articles/5/1097/2020/>, 2020a.
- 875 Schelbergen, M., Kalverla, P. C., Schmehl, R., and Watson, S. J.: Clustering wind profile shapes to estimate airborne wind energy production, *Wind Energy Science Discussions*, 2020, 1–34, <https://doi.org/10.5194/wes-2019-108>, <https://www.wind-energ-sci-discuss.net/wes-2019-108/>, 2020b.
- Schmehl, R., Noom, M., and van der Vlugt, R.: Traction Power Generation with Tethered Wings, pp. 23–45, Springer Berlin Heidelberg, Berlin, Heidelberg, https://doi.org/10.1007/978-3-642-39965-7_2, https://doi.org/10.1007/978-3-642-39965-7_2, 2013.
- 880 Sempreviva, A. M. and Gryning, S.-E.: Humidity fluctuations in the marine boundary layer measured at a coastal site with an infrared humidity sensor, *Boundary-Layer Meteorology*, 77, 331–352, <https://doi.org/10.1007/BF00123531>, 1996.
- Skamarock, W., Klemp, J., Dudhia, J., Gill, D., Barker, D., Duda, M., Huang, X., Wang, W., and Powers, J.: A description of the advanced research WRF version 3, Tech. Rep. NCAR/TN–475+STR, NCAR - National Center for Atmospheric Research, Boulder, Colorado, USA, <http://n2t.net/ark:/85065/d72n51q1>, 2008.
- 885 Sommerfeld, M., Crawford, C., Monahan, A., and Bastigkeit, I.: LiDAR-based characterization of mid-altitude wind conditions for airborne wind energy systems, *Wind Energy*, 22, 1101–1120, <https://doi.org/10.1002/we.2343>, 2019a.
- Sommerfeld, M., Dörenkämper, M., Steinfeld, G., and Crawford, C.: Improving mesoscale wind speed forecasts using lidar-based observation nudging for airborne wind energy systems, *Wind Energy Science*, 4, 563–580, <https://doi.org/10.5194/wes-4-563-2019>, <https://www.wind-energ-sci.net/4/563/2019/>, 2019b.
- 890 Stull, R.: *An Introduction to Boundary Layer Meteorology*, Atmospheric and Oceanographic Sciences Library, Springer Netherlands, <https://books.google.ca/books?id=eRRz9RNvNOKC>, 1988.
- van der Vlugt, R., Bley, A., Noom, M., and Schmehl, R.: Quasi-steady model of a pumping kite power system, *Renewable Energy*, 131, 83 – 99, <https://doi.org/10.1016/j.renene.2018.07.023>, <http://www.sciencedirect.com/science/article/pii/S0960148118308206>, 2019.
- Wächter, A. and Biegler, L. T.: On the implementation of an interior-point filter line-search algorithm for large-scale nonlinear programming, *Mathematical Programming*, 106, 25–57, <https://doi.org/10.1007/s10107-004-0559-y>, <https://doi.org/10.1007/s10107-004-0559-y>, 2006.
- 895

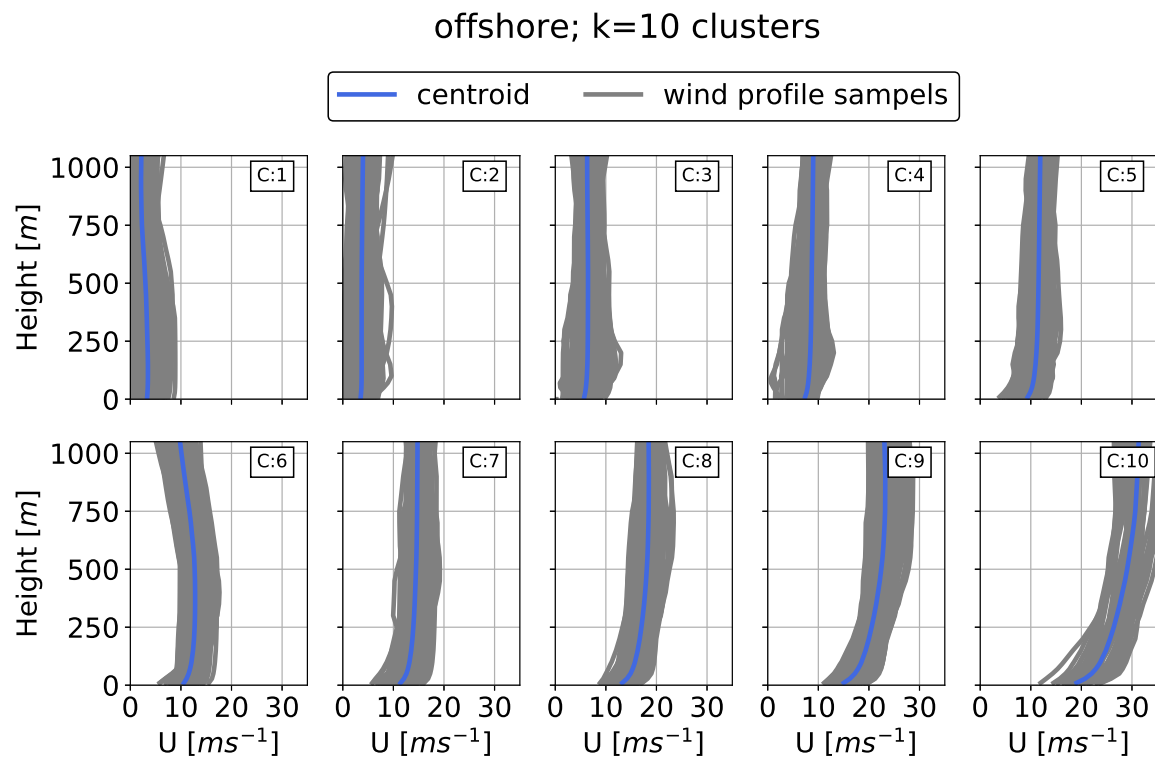


Figure A1. Clustered offshore wind velocity profiles (here shown as wind speed profiles). The average profile or centroid is shown in blue while all the assigned profiles are shown in grey.

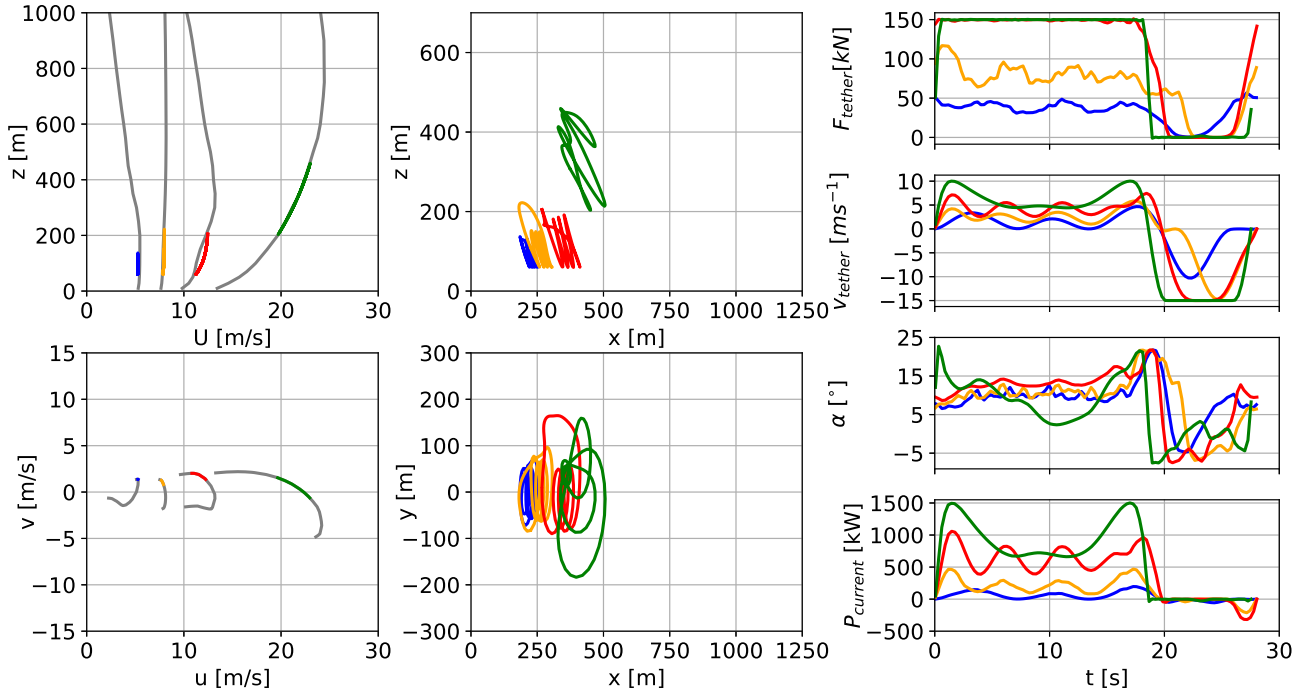


Figure A2. Representative wind speed profiles (left, top), and hodograph (top view) of wind velocity up to 1000 m (left, bottom). The deviation of the colored lines is caused by the approximation of discrete data points with Lagrange polynomials. Trajectories (center) in side and top view. Temporal variations of tether force F_{tether} (right, 1st from top), tether speed v_{tether} (right, 2nd from top), angle of attack α (right, 3rd from top) and instantaneous power $P_{current}$ (right, bottom) optimized based on clustered offshore wind speed profiles for a ground-generation aircraft with a wing area of $A_{wing} = 20 \text{ m}^2$.

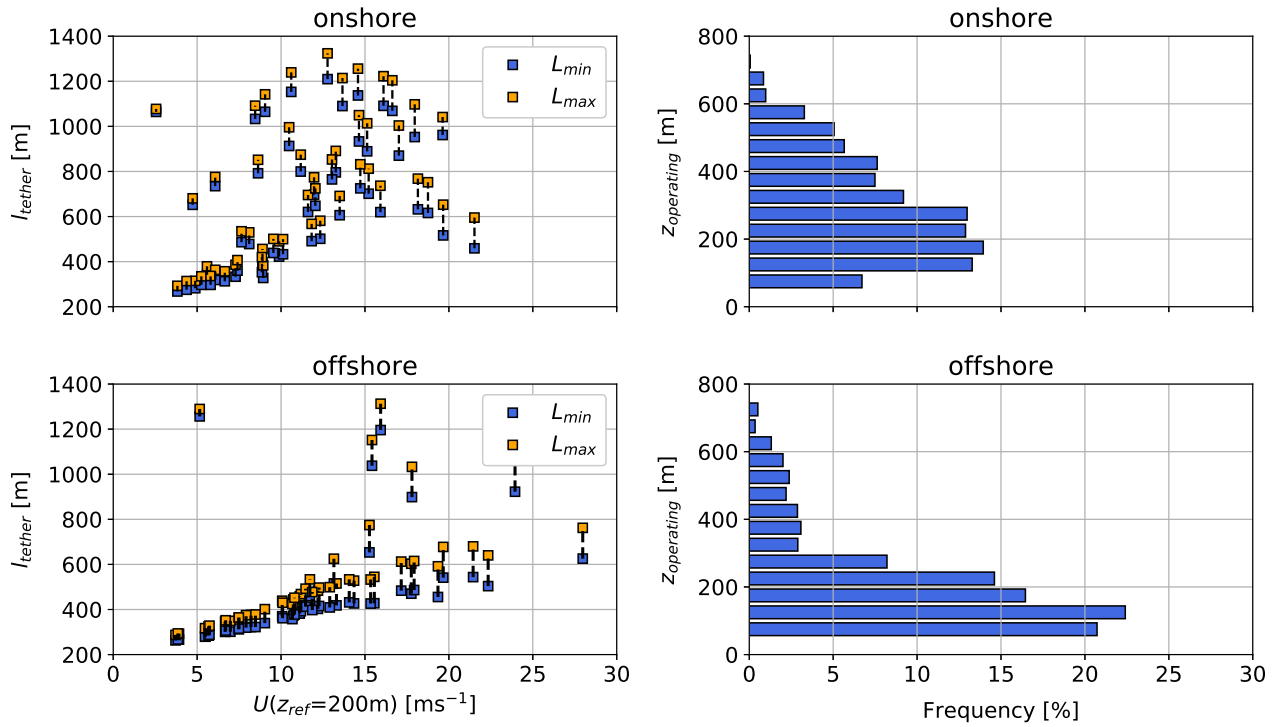


Figure A3. Tether length range (left) over reference wind speed $U(z_{ref} = 200 \text{ m})$ and frequency distribution of operating altitude (right) based on $k=20$ onshore (top) and offshore (bottom) clusters for a ground-generation aircraft with a wing area of $A_{wing} = 50 \text{ m}^2$.

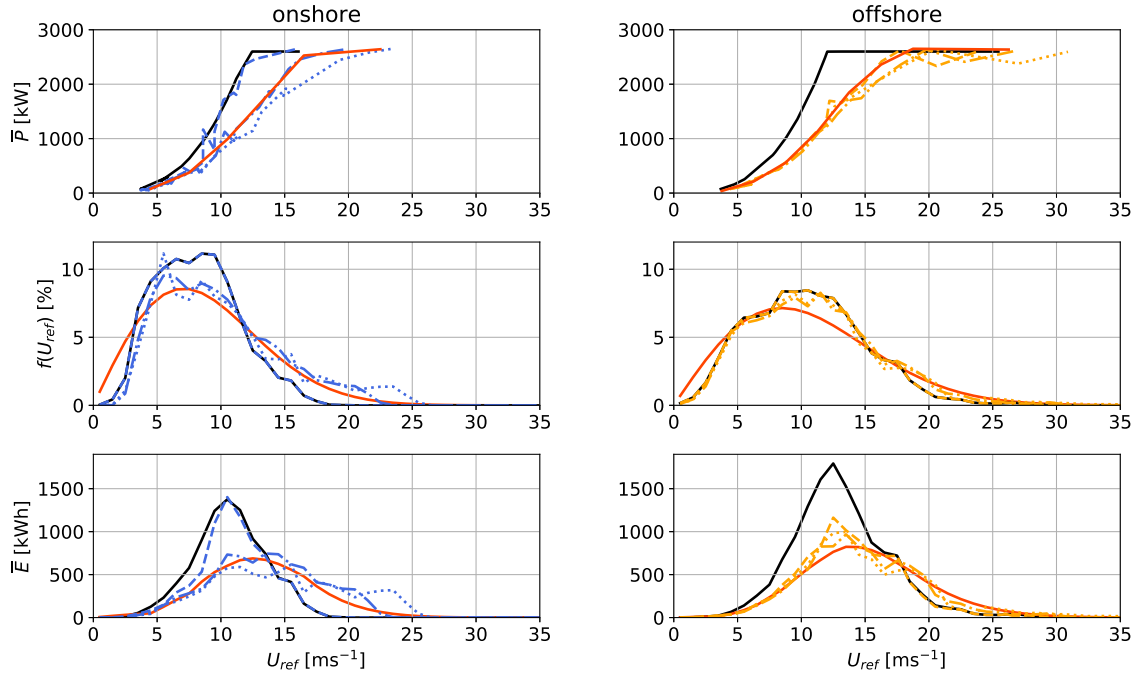
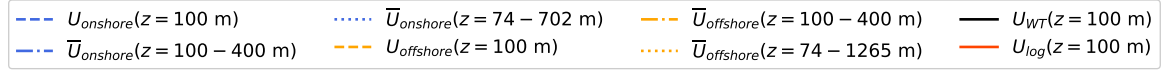


Figure A4. AWES power curves onshore (top left, blue) and offshore (top right, orange) for $A_{wing} = 50 \text{ m}^2$ over various reference wind speed height definitions (dashed lines: fixed height $z = 100\text{m}$; dash-dotted lines: fixed height range $z = 100 - 400 \text{ m}$; dotted lines: average wind speed along operating trajectory) based on 3 profiles for each of the $k=20$ clusters. Compared to WT (black) with same rated power at a hub height of $z_{WT} = 100 \text{ m}$ and AWES (red) for logarithmic wind speed profiles ($z_0 = 0.1$ onshore and $z_0 = 0.001$ offshore). Annual wind speed probability distribution (center) based on WRF simulation and Rayleigh distribution (red) with $U_{ave} = 10 \text{ ms}^{-1}$ (onshore) and 12 ms^{-1} (offshore) for reference. Energy production distribution (bottom) shows the distribution of annual produced energy over wind speed which is the product of power and wind speed probability distribution. Integrating this product results in the AEP.

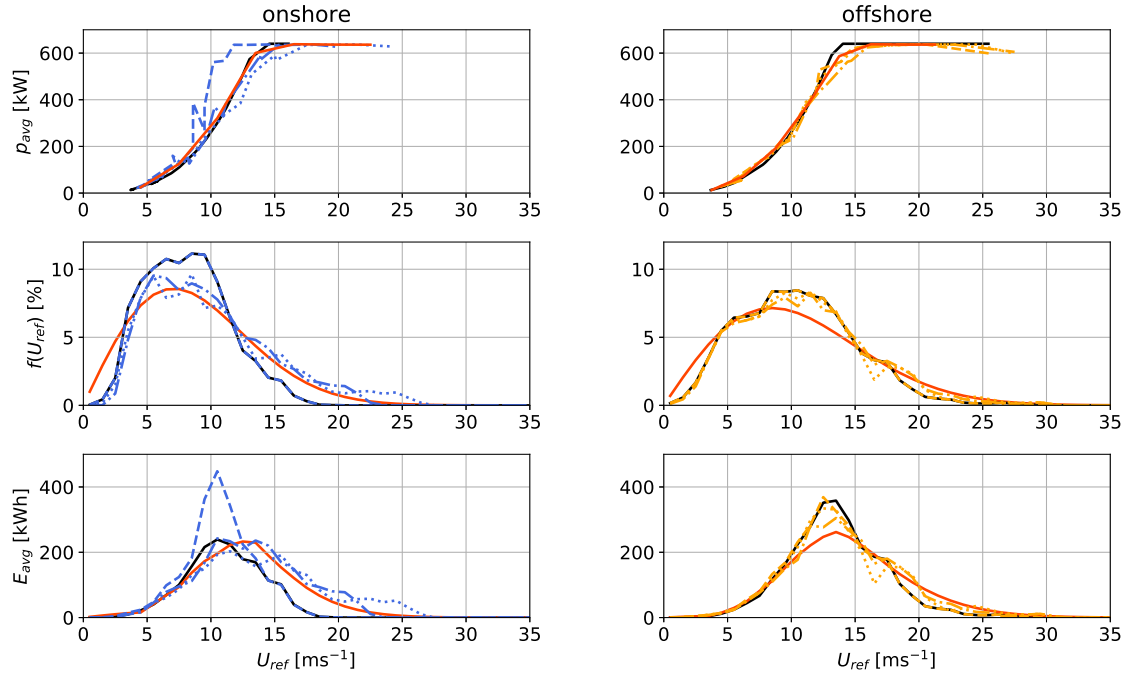
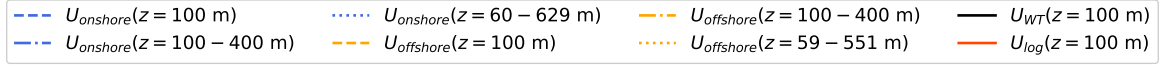


Figure A5. AWES power curves onshore (top left, blue) and offshore (top right, orange) for $A_{wing} = 50 \text{ m}^2$ over various reference wind speed height definitions (dashed lines: fixed height $z = 100\text{m}$; dash-dotted lines: fixed height range $z = 100 - 400 \text{ m}$; dotted lines: average wind speed along operating trajectory) based on 3 profiles for each of the $k=20$ clusters. Compared to WT (black) with $c_p^{WT} = 0.3$ and same rated power at a hub height of $z_{WT} = 100 \text{ m}$ and AWES (red) for logarithmic wind speed profiles ($z_0 = 0.1$ onshore and $z_0 = 0.001$ offshore). Annual wind speed probability distribution (center) based on WRF simulation and Rayleigh distribution (red) with $U_{ave} = 10 \text{ ms}^{-1}$ (onshore) and 12 ms^{-1} (offshore) for reference. Energy production distribution (bottom) shows the distribution of annual produced energy over wind speed which is the product of power and wind speed probability distribution. Integrating this product results in the AEP.